Improved Energy Reconstruction with Generalized Particle Decays by Applying Multiple Constraints

By

Justin Anguiano

Submitted to the graduate degree program in Department of Physics and Astronomy and the Graduate Faculty of the University of Kansas in partial fulfillment of the requirements for the degree of Master's in Computational Physics and Astronomy.

Prof. Graham Wilson, Chairperson

Committee members

Prof. Alice Bean

Prof. Chris Rogan

Date defended: October 06, 2017

The Thesis Committee for Justin Anguiano certifies
that this is the approved version of the following thesis :

Improved Energy Reconstruction with Generalized Particle Decays by Applying Multiple Constraints

Prof. Graham Wilson, Chairperson

Date approved: November 13, 2017

Abstract

Mass constrained fitting is a technique that improves jet energy resolution. The fit is performed by assigning a well-known mass to a decaying particle and minimizing a χ^2 consisting of the constituent particle's measured parameters. This technique is utilized in an abstract frame work which applies multiple constraints to arbitrary multi-generational particle topologies. The software is constructed with the ability to both fit designated particles and automate the analysis of all particle parameters post-fit, including Monte Carlo information. The energy reconstruction is tested for single and multiple constraints in the decays of $J/\psi \to \mu^+\mu^-$, $\pi^0 \to \gamma\gamma$, $\eta \to \pi^+\pi^-\gamma$, and $\eta \to \pi^+\pi^-\pi^0$.

The code repository can be found at https://github.com/Jphsx/constrainedFitter.git

Contents

Chapter 1

Introduction

The International Linear Collider (ILC) is a high-luminosity linear electron-positron collider based on 1.3 GHz superconducting radio-frequency accelerating technology. Its centre-of-mass-energy range is 200–500 GeV (extendable to 1 TeV) [1]. The ILC will provide new opportunities for direct Higgs measurements. One of the new channels in which to explore the Higgs, is the energy reconstruction of the Higgs through hadronic decay modes. The Higgs mass as well as couplings can be directly measured through hadronic visible decays which can potentially benefit from constraints. If the particles parameters and errors are well measured, the energy and momentum measurements can be improved by applying constraints to the system. A single particle may decay into a set of particles, the second generation of particles may also decay, resulting in another generation of particles. If the final state particles can be identified, then the invariant mass of the particle system can be set to an exact value. The final state particles under the mass constraint can be adjusted in terms of energy and momentum, such that a χ^2 constructed from the constituent parameters is minimized. So, by applying mass constraints to a multi-generational set of particle decays, the reconstructed energy of the original parent particle, along with the parameters of its descendants, can be more precisely estimated. The energy resolution also scales with the number of constraints applied to the system of particles. This paper details a MarlinKinfit processor that applies any number of mass-constraints to multi-generational decay consisting of any mixture of charged and neutral particles. The processor is tested with four basic use-cases. Single mass constraints are applied to a system of single particle decays of one type (charged or neutral) for 20 GeV $J/\psi \rightarrow \mu^+\mu^-$ and 10 GeV $\pi^0 \rightarrow \gamma\gamma$. Here the di-muon system is constrained to the J/ψ mass and the di-photon system is constrained to the π^0 mass. A single mass constraint is also tested on a mixture of charged and

neutral particles for a 20 GeV decay of $\eta \to \pi^+\pi^-\gamma$ where the final state is constrained to the η mass. The final data set tested in the processor is a 20 GeV $\eta \to \pi^+\pi^-\pi^0$ decay. This particle set has a two generation decay with two possible mass constraints, or a 2C fit. The final state of the two generation decay is $\pi^+\pi^-\gamma\gamma$ where the four final state particles are constrained to the η mass and the di-photon subset is constrained to the π^0 mass. The 1C fit is also contrasted with the 2C fit, where the 1C fit the $\pi^+\pi^-\gamma\gamma$ four particle final state is constrained to the η mass.

1.1 The International Linear Collider

ILC is an e^+e^- linear collider whose main motivation in design is to carry out precision Higgs physics. The collider is planned to start with a center of mass energy of 250 GeV with planned upgrades in luminosity and center of mass energy up to 500 GeV. ILC offers a great opportunity to have a clean reconstruction of the Higgs Boson, particularly in the hadronic decay channels due to the lack of QCD background. The collider is planned to be 31km long, as pictured in Figure 1.1, with e^+e^- pulsed bunch trains. The bunches are separated by about 300 ns, with each bunch containing about 2×10^{10} particles. The particles interact with a cross section on the order 100's of nb and are expected to reach a total integrated luminosity of 2.5 ab^{-1} [2] [3]. The main physics motivation for the ILC is to produce precision Higgs measurements, such as a direct measurement of the branching ratios and precision measurement of Higgs couplings, such as, ZZH or Higgs self coupling.

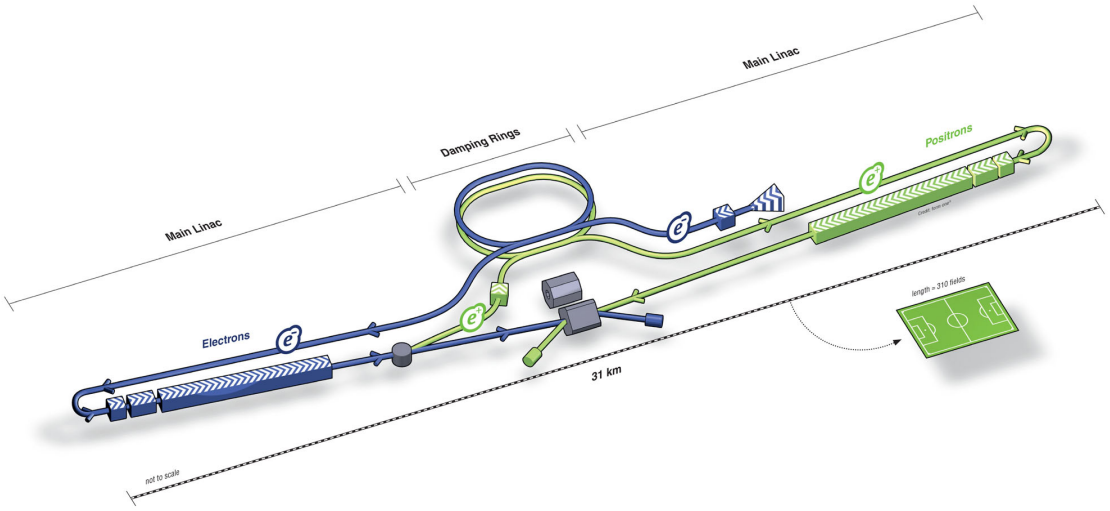

Figure 1.1: Illustration of ILC concept with two linear accelerators meeting at a center point that contains two interchangeable detectors.

1.2 International Large Detector

There are two separate detectors designed for ILC. They are designed with a “push-pull" concept which gives the option for the detectors to be swapped out at the interaction point (IP). The two detectors are the International Large Detector (ILD) and the Silicon Detector (SiD). The main differences between the detectors are the tracking design and detector size. ILD is centered on a gas based tracking system which provides bubble chamber-like continuous charge particle reconstruction, while SiD uses silicon based tracking system that connects tracks based on fewer hits. The detector used for the following constrained fitting is the ILD.

ILD is composed of several complementary layers, as pictured in Figure 1.2, each layer has a specific role in reconstruction. Starting from the innermost layer, the Vertex Detector (VTX), records the initial hits from tracks emerging from the IP and displaced vertices. The vertex detector is encased in the Time Projection Chamber (TPC). The TPC is the tracking mechanism that records the paths of charged particles by measuring the ionization trails produced by charged particles interacting with the gas in the tracking medium. Surrounding the TPC, is a silicon layer for precision measurements of track endpoints. The next two layers are the Electromagnetic Calorime-

ter (ECAL) and the Hadronic Calorimeter (HCAL). These calorimeters stop the majority of outgoing particles and measure the energy deposited. The ECAL is oriented towards precision photon measurement and the HCAL collects the majority of heavier hadrons. Outside the main detector subsystems is the solenoid that produces the 3.5 T uniform magnetic field in the detector. Finally, the outermost region is the muon chamber which records the tracks of the muons exiting the detector.

1.2.1 Detector Subsystems

The Vertex Detector has three concentric layers spaced approximately 16mm apart. Each side of each layer is covered with pixel sensors which allows up to 6 track hits within a radius of 15-60 mm from the interaction point. The performance of the vertex detector is expected to yield a spatial resolution near the IP better than 3μm [4].

The TPC is an argon gas based detector composed of an Ar-CF_4(3%)-isobutane(2%) mixture. Charged particles ionize the gas in the radial region from $\sim$ 300mm to $\sim$ 1800mm [4]. The ionized particles drift to the endplates where they can be reconstructed and identified based on specific energy loss dE/dx. The endplates can record up to 224 hits per track and have a single space point resolution of up to $\sim$ 50μm [4].

The ECAL is composed of 29 silicon-tungsten layers. The first 20 layers have thinner tungsten layers at 2.1 mm wide and the outer layers are twice as thick. The active silicon layers are 5x5 mm^2 pixels [5].

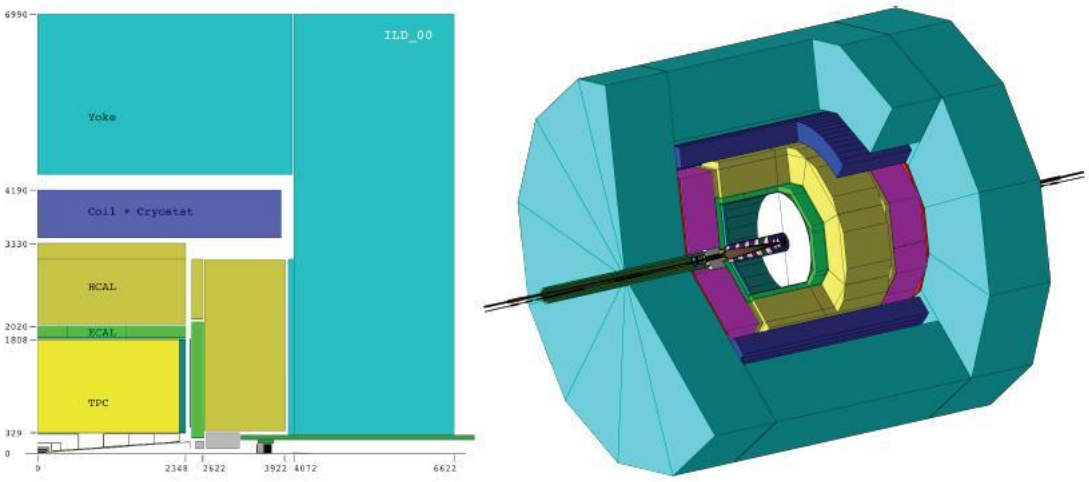

Figure 1.2: (Left) A cross section quadrant of the projected ILD design along with estimated dimensions. The detector geometry is defined such that the transverse $(x-y)$ plane is orthogonal to the beam pipe (Right) The external detector perspective to illustate the cylindrical design of ILD.

Chapter 2

Particle Reconstruction

The main reconstruction method for ILD is Particle Flow. This technique focuses on the reconstruction of the four momentum of the invdividual particles seen in the detector. Particle flow reconstruction requires precision tracking and a highly granular calorimeter. A highly granular calorimeter gives a stronger ability to distinguish between energy clusters yielding a better ability to differentiate particles. The quality of particle reconstruction is reliant on the software performance which entails the necessity to associate energy clusters to tracks and differentiate between energy deposits in the calorimeters. The reconstruction process is mainly a sequence of clustering particle flow algorithms(PFA) called PandoraPFA [5]. These algorithms focus on associating tracks with energy clusters, and separating or merging energy clusters to differentiate between electromagnetic and hadronic deposits. The main limitations of the PandoraPFA performance is associated with the improper identification/merging/separation of clusters, for example, merging a neutral hadron deposit with a separate cluster, or separating cluster fragments into neutral hadrons will yield the incorrect number of reconstructed particles measured at the wrong energies. The Pandora algorithm is composed of eight stages in which the final stage the particles are stored in LCIO, a persistency framework for linear collider simulation studies [6].

- Track selection/topology
  - Tracks from kinks and neutral hadron decays are identified.
- Calorimeter hit selection and ordering
  - Isolated hits are removed, and the remaining clusters are turned into pseudo-layers that contain information about the detector geometry

- Clustering
  - Starting from tracks projected onto the inner ECAL, hits are associated into clusters based on cones extending from each hit. The cones are oriented in the initial or current direction. Hit cones that overlap are aggregated into a cluster, otherwise hits form new clusters.
- Topological cluster merging
  - Merges isolated clusters, that do not have an associated track, with clusters that have an associated track.
- Statistical re-clustering
  - Performs cluster separation to adjust energy clusters such that they have E/p consistency with their associated track.
- Photon recovery
  - Uses photon identification algorithms that identify photon clusters based on the longitudinal energy deposition profile.
- Fragment removal
  - Separated neutral hadron clusters are attempted to be merged with charged hadron clusters to improve track consistency.
- Formation of particle flow objects
  - The Particle Flow Objects (PFOs) are formed, tracks are officially matched with the energy clusters, and the resulting reconstructed particles are written out in the LCIO format.

Once the particle flow objects have been constructed and stored in LCIO, they are extracted by secondary processors for calibration and constrained fitting where the PFOs can be refined.

Chapter 3

Constrained Fitting

Constrained fitting is a mathematical method that can be used to improve the measurement of particles. Introducing additional information, or applying constraints, can help to achieve better accuracy and precision in a measurement. This fitting technique can be performed with the Lagrange multiplier method

$$\chi^2 = \sum_i \frac{(\xi_i - \hat{\xi}_i)^2}{\sigma_i^2} + \sum_j \lambda_j C_j \tag{3.1}$$

where ξ_i are a set of measured parameters with approximately gaussian error σ_i and $\hat{\xi}$ is a close approximation to the true value of the parameter ξ. C_j are the related constraints and λ_j are the lagrange multipliers. The minimization of the χ^2 w.r.t to the estimator $\hat{\xi}_i$ is given by

$$\frac{\partial \chi^2}{\partial \hat{\xi}_i} = 0 \quad \text{and} \quad \frac{\partial \chi^2}{\partial \lambda_j} = 0 \tag{3.2}$$

Solving this set of equations for $\hat{\xi}_i$ yields the optimal set of parameters that satisfy the χ^2 within the given errors. This new estimator should hopefully be closer to the true value than the measurement. Experimentally the appropriate constraints to particle reconstruction are mass constraints, which requires a set of particles from a decay to have a precise invariant mass. Thus in the minimization, the energy and momentum of the constituent particles is adjusted in a way such that the set of particles remains consistent with a known invariant mass. Other constraints are also possible, like, requiring constituent particles to be produced at a common vertex, or vertex constraint.

Chapter 4

MarlinKinfit & Local Parameterizations

MarlinKinfit is an object–oriented kinematic fitting package [13]. The tool does kinematic fitting using the method of Lagrange multipliers. The software relies on three major components: a fitting engine to set up a system of equations and solve them, a constraint on the fit, and a FitObject. There is a FitObject for each particle in each event and this object determines the local parameterization for that type of particle. The initial measured parameters and covariance matrices are stored in FitObjects [13]. The processor is written with the expectation to be generalizable to arbitrary parameterizations for both neutral and charged particles. However, FitObjects must be implemented specifically supporting the local parameterization. Similarly, the deliverable four-vector error matrix is hardcoded to support the local parameterization. This code version only supports the neutral particle parameteriztion (E, θ, ϕ) and the track parameterization (κ, θ, ϕ) where $\kappa = q/P_T$. To support any arbitrary parameterization, the FitObjects could be abstracted to their base class BaseFitObject. The polymorphic child class could then be defined in the input XML.
The parameterization used for the analysis is (κ, θ, ϕ) for charged particles due to the requirements of LeptonFitObject. The other parameterization is (E, θ, ϕ) for neutral particles based on the input requirements of JetFitObject. The most natural parameterization for tracks is the 5 helix parameters using TrackParticleFitObject, but the class in its current state, along with time constraints in project implementation, only support vertex fitting with only charged tracks. The TrackParticleFitObject fit would not converge when combined with other FitObjects and constraints. Fortunately, LeptonFitObject accounts for the full covariance matrix of the five parameter track so track information is not lost in the change of parameterization.

4.1 Charged Particle Reconstruction

A charged particle traveling through the uniform magnetic field in the detector leads to helical track trajectories. These tracks are reconstructed via hits in the vertex detector which are connected with a more continuous sequence of hits in the TPC. The kinematics of the charged particle tracks can be described fundamentally from the the Lorentz Force equation

$$\vec{F} = q(\vec{E} + \vec{v} \times \vec{B}) \tag{4.1}$$

where q is the charge, $\vec{E}$ is the electric field, and $\vec{B}$ is the magnetic field defined as $\vec{B} = B\hat{z}$. Using $\vec{F} = d\vec{p}/dt$ and setting $\vec{E} = 0$, the Lorentz equation reduces to

$$\frac{d\vec{p}}{dt} = q\vec{v_T}B \tag{4.2}$$

where $\vec{v_T}$ is the transverse velocity in the x-y plane. From rotational kinematics we can express this equation in terms of transverse momentum and radius of curvature R.

$$p_T = qBR \tag{4.3}$$

The transverse momentum is extracted from the track by directly measuring the radius of curvature in the tracker. Some of the initial hits from the track are extracted from the vertex detector, while the rest of the track, up to 224 points in space, are reconstructed in the TPC. The Radius of Curvature R is the center of the arc produced in the trajectory projected in the (r, ϕ) plane. After the initial momentum reconstruction of the track, a mass assumption is made and assigned to the particle. The assumption is based on the specific energy loss of the particle passing through the detector medium.

The track reconstruction is done with two parameterizations. The natural parameterization is the helix frame, however the fitting is performed with a separate local parameterization due to software limitations and time constraints. The helix consists of five parameters $(d_0, \phi_0, \Omega, z_0, \tan\lambda)$. d_0 and

z_0 are the points of closest approach to some reference point (likely the IP at $(0,0,0)$) in the (r,ϕ) and (r,z) planes respectively. ϕ_0 is the angular orientation in the (r,ϕ) plane with respect to the reference point (origin) to the point of closest approach. Ω is the inverse signed curvature of the track $\Omega \equiv 1/R$. The sign of the curvature is positive if the rotation about $\hat{z}$ is clockwise and negative for counter-clockwise. The last parameter is $\tan\lambda$, this is the tangent of the dip angle, where the dip angle λ is the angle from the transverse axis in the (r,z) plane. The helix parameters are measured by fitting the track hits. In the (r,ϕ) plane, the parameters R, d_0, and ϕ_0 can be obtained. The projected track trajectory in the (r,ϕ) plane is circular and can be approximated with a quadratic fit. So, for a set of measurements y_n along the circular path, we can approximate the helical projection (in a cartesian space) from the equation of a circle

$$(y-y_0)^2 + (x-x_0)^2 = R^2 \tag{4.4}$$

if the track momentum is not too small such that $R^2 \gg (x-x_0)^2$ then we can make a linear approximation for the solution to y

$$y \approx (y_0 + R - \frac{x_0}{2R^2}) + \frac{x_0}{R}x - \frac{1}{2R^2}x^2 \tag{4.5}$$

The expression for y can be approximated with the quadratic model in

$$y = a + bx + cx^2 \tag{4.6}$$

where the coefficient c can be measured from a least squares fit, where $c = 1/2R^2$ [9]. Following the fit, the inverse radius of curvature Ω can be directly calculated, and the other parameters can be extracted from the fitted model. The other parameters z_0 and $\tan\lambda$ are calculated based on measured the drift time measured at the tracker endplates. The tangent of the dip angle is measured by calculating the ratio of longitudinal and transverse momenta.

4.1.1 Charged Particle Error Model

The track errors are represented in a 5×5 helix parameter covariance matrix. The track errors are dominated by three sources: random errors from measurement by the detector, error due to multiple scattering, and error due to energy loss. The errors contribute to multiple parameters so the track errors are correlated because of the reliance on the radius of curvature. Energy loss due to the passage of charged particles through a material causes a decrease in the momentum, this effect contributes to the overall momentum resolution of the charged particle. The energy loss depends on the stopping power of the medium that the particle traverses. This behavior is characterized by the Bethe equation for specific energy loss [8]

$$-\frac{dE}{dx} = Kz^2\frac{Z}{A}\frac{1}{\beta^2}\Big[\frac{1}{2}\ln\frac{2m_e c^2\beta^2\gamma^2 W_{max}}{I^2} - \beta^2 - \frac{\delta(\beta\gamma)}{2}\Big] \tag{4.7}$$

Where W_{max} is the maximum energy transfer in a single collision given by [8]

$$\frac{2m_e c^2\beta^2\gamma^2}{1 + 2\gamma m_e/M + (m_e/M)^2} \tag{4.8}$$

M is the charged particle mass, m_e is the mass of the electron, β and γ are relativistic kinematic variables. Z is the atomic number of the absorber, A is the atomic mass of the absorber, z is the charge of the incident particle, K is a constant 0.307075 MeV mol^{-1} cm^2, I is mean excitation energy, and $\delta(\beta\gamma)$ is a density effect correction to ionization energy loss.

The momentum of a charged particle is ultimately measured by the radius of curvature, which is related to the inverse of the transverse momentum of the particle. The detector and multiple scattering errors are directly accountable for resolution on the particles momenta. The curvature error is expressed with $\kappa = 1/R$ by [8]

$$(\delta\kappa)^2 = (\delta\kappa_{res})^2 + (\delta\kappa_{ms})^2 \tag{4.9}$$

$\delta\kappa_{res}$ is the finite resolution in the detector measurement and $\delta\kappa_{ms}$ is the error due to multiple scattering. The resolution term can be expressed in terms of the track information [8]

$$\delta\kappa_{res} = \frac{\epsilon}{L'^2}\sqrt{\frac{720}{N+4}} \tag{4.10}$$

where ϵ is the measurement error of each point in the track, L'^2 is the arc length of the track helix, and N is the number of points measured along the track. The points along the track are also assumed to be equally spaced. The multiple scattering term can be approximated with [8]

$$\delta\kappa_{ms} \approx \frac{(0.016)(GeV/c)z}{Lp\beta\cos^2\lambda}\sqrt{\frac{L}{X_0}} \tag{4.11}$$

where z is the charge of the track, L is the track length, p is momentum, λ is the dip angle, and X_0 is the radiation length in the scattering medium. The angular resolution of the tracks can be propagated through the curvature errors, and is also dominated by multiple scattering.

4.2 Photon reconstruction

Electromagnetic shower development is described using the Grindhammer-Peters model [10]. A photon cluster can be approximated to the first order using a model with shower development through a homogeneous material. The exact shape of shower structures emerge from the sampling methods, material, and detector geometry. The spatial energy distribution is given by

$$dE(\vec{r}) = Ef(t)dt\,f(r)dr\,f(\phi)d\phi \tag{4.12}$$

where $f(t)$ is the longitudinal shower development with t in units of increasing radiation lengths and is modeled with a Gamma distribution. The azimuthal components is distributed uniformly such that $f(\phi) = 1/2\pi$. The longitudinal development $f(t)$ can be further described by

$$\left\langle \frac{1}{E}\frac{dE(t)}{dt} \right\rangle = f(t) = \frac{(\beta t)^{\alpha-1}\beta\exp(-\beta t)}{\Gamma(\alpha)} \tag{4.13}$$

where α and β are the shower shape and scale parameters respectively. The radial distribution $f(r)$ is based on a two parameter ansatz based on a Monte Carlo calculation of photon showers in lead glass [11].

4.2.1 Photon error models

The photon reconstruction is dependent on how the photon interacts with the calorimeter. At very low energies the photoelectric effect dominates, at energies around ~ 1 keV to 1 GeV the Compton scattering effect is prominent, and at energies above 1 GeV pair production dominates. In the traditional calorimetric approach, energy resolution is given by

$$\frac{\sigma_E}{E} = \frac{\alpha}{\sqrt{E}} \oplus \beta \tag{4.14}$$

Here E is the photon energy in GeV, and resolution is a function of energy. The first term is the stochastic term based on statistical fluctuations where $\alpha = 0.18$. The second term is the constant term with $\beta = 0.01$. The constant term dominates the energy resolution at high energies and receives contributions from effects like miscalibration or leakage [5]. The threshold energy in which the leading error term matches the error contribution from the second term is an excessively high energy ~ 300 GeV. All simulated photon energies are significantly less than this threshold energy, so, the β term is neglected in this study.

The angular resolution for photons is also dependent on photon energy. If the energy resolution scales as $1/\sqrt{E}$ and the average shower profile stays the same as a function of energy, then the spatial resolution should also scale as $1/\sqrt{E}$ [12]. However local parameters require the resolution to be defined in terms of θ and ϕ. So, naively it is assumed that the angular resolution for a photon is subject to the same scaling as the spatial resolution, thus, $\sigma_{\theta,\phi} \sim 1/\sqrt{E}$. When a photon interacts with the calorimeter it produces a shower of particles which typically is an electron-positron pair that also interacts with the calorimeter producing more photons. This effect chains together producing a longitudinally developing shower. The electrons and positrons produced are

still subject to the magnetic field present in the calorimeter, so, the bending of the electron and positron trajectories can obscure the original direction. Since the charged particle multiplicity should be correlated with the incident photon energy, i.e. more electron-positron pairs at higher energies, then the photon angular resolution should be a function of photon energy. Also for simplicity the different angles for photon resolution are approximated by the same model, which is given by

$$\sigma_{\theta,\phi} = \frac{0.001}{\sqrt{E}} \tag{4.15}$$

The coefficient is empirically based on the expectations from the angular resolution of the granularity of the calorimeter. A resolution on the order of 1mrad is estimated.

Chapter 5

General Mass Constraint Fitter

The processor begins with a decay hypothesis, that is, some particle X decays into a set of constituent particles which may be a mixture of both charged and neutral particles. The standard reconstruction, from PandoraPFA, produces the particles that are the input for the processor. The reconstructed particles may be a superset of those needed to satisfy the decay hypothesis. In this case, every possible combination of particles that satisfy the decay hypothesis are fit with a mass constraint. The subset of particles that produce the highest fit probability is the subset of particles that is selected as the "correct" mass hypothesis. If the reconstructed set of particles is smaller than the necessary amount of particles needed to satisfy the decay hypothesis, the event is then rejected. The set of particles and fit information is stored in an output LCIO file. The particles relevant parameters, errors, and pull distributions are optionally stored in the output ROOT object TTree [7] . If the Monte Carlo particle information is available in the event, the Monte Carlo particles are matched with the set of fitted particles from the mass constraint. All parameters and pull distributions related to the Monte Carlo particles are also placed onto the output TTree. The working pipeline for the fitter is shown in Figure 5.1.

5.1 Processor Input

There are two types of input for the processors, XML and LCIO. The XML steering files contain all of the event specific information and is described in detail in Appendix B, an example is also given in Appendix C . The LCIO input for each processor uses a combination of three possible types of collections; ReconstructedParticle, Track, and MCParticle. The ReconstructedParticle collection

contains the particle's four-vector information, charge, particle ID number, and covariance matrix. The tracks or clusters associated with the particle are also available. The Track collection holds the five parameter helix information, specific energy loss, and track covariance matrix. The MCParticle collection holds all of the Monte Carlo four-vector information, and links to the associated ancestor or descendant Monte Carlo particles.

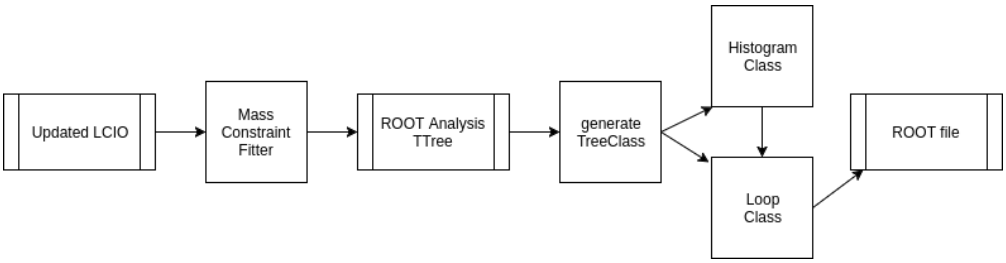

Figure 5.1: A flow chart of the events through the initial mass constraint fitter and the pipeline that follows the initial output producing more detailed analysis files.

5.2 Secondary processors

The processor pipeline includes complementary processors, illustrated in Figure 5.2. The three processors are a MCParticle filter and two calibration processors that adjust the track and photon parameters.

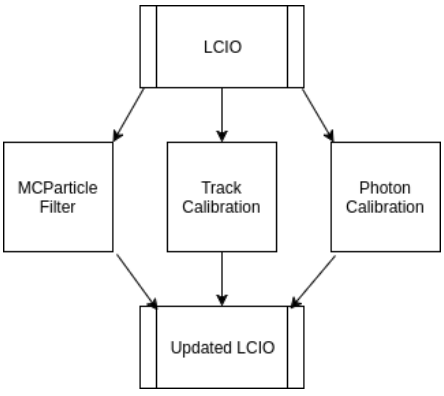

Figure 5.2: A flow chart of the event input into the secondary processors where the initial input information is corrected and updated.

5.2.1 MCParticleFilter

The MCParticleFilter is a processor that reads in the MCParticle collection and filters out all secondary particles following the first generation of particles in the parent decay. These particles are then stored in a new subset of MCParticle. The MCParticle collection contains every particle due to decay or interaction with the detector. Each particle also has its true energy before it is smeared by measurement in the detector. Since each decay is prompt, the criteria for selecting the first generation is that their primary vertex is the interaction point. The motivation for filtering the MCParticle collection is to provide a cleaner set of generator particles to match and compare with the corresponding reconstructed set of particles in an event within the MassConstraintFitter.

5.2.2 TrackCalibration

The TrackCalibration processor reads in the track collection MarlinTrkTracks and adjusts the covariance matrix elements by a scale factor unique for each of the five track parameters. The tracks and new calibrated covariance matrix are then saved to a new CalibratedTracks collection.

5.2.3 PhotonCalibration

The PhotonCalibration processor reads in PandoraPFOs and adjusts the photon energy by some scale factor, while preserving the direction of the original photon. The processor also has the option to resimulate the photon direction based on the MCParticle photon directions. If the angles are to be resimulated, the generator level orientation for θ and ϕ is taken from the MCParticle collection and gaussian random deviates for new values of θ and ϕ are drawn to replace the original reconstructed direction. The random variate distributions are centered on the generator values and the width is characterized by the photon angular error model $\sigma \approx 0.001/\sqrt{E}$ [mrad]. There is no covariance matrix initially in the collection, so no errors are adjusted. The errors for the photon are calculated in the MassConstraintFitter.

5.3 Combinatorial Fitting

For a given decay being analyzed, a parent particle can decay into any combination of particles such that the true decay is represented by

$$P \rightarrow \sum_{i=0}^{k} N_i + \sum_{j=0}^{r} C_j \tag{5.1}$$

where parent P decays into k neutral particles, N_i, and r charged particles, C_i. However in the reconstruction there are often more or less particles reconstructed than the exact combination of r, and k. This gives rise to combinatorial problems with particle selection. If n neutral particles are reconstructed and m tracks are reconstructed then the possible solutions are given by

$$C_{k,r}^{n,m} = \binom{n}{k}\binom{m}{r} \tag{5.2}$$

which has the potential to give rise to a large set of possible solutions. Each possible combination of particles is calculated and fitted. The set of particles with the highest fit probability is kept as the best solution, which is not necessarily the correct set of particles. For the charged tracks, the mass assumptions from the true set are imposed on each track. For decays with multiple charged masses, the combinations increase significantly because the m tracks are now fitted with every possible mass assumption. One cut, however, to decrease running and fitting time, is to check that the set of particles has a net charge consistent with the parent charge.

For a given decay, there may be an opportunity to apply more than a single constraint. A parent particle may decay to a set of particles which also may decay into another set of particles. If multiple mass constraints are applied, one for each generation of particles the fit can be improved. The decay of $k+r$ particles can be constrained to the mass of the parent P. Here there may be subsets of the P decay that can be constrained to secondary masses m. An example of this (to be analyzed later) is $\eta \rightarrow \pi^+\pi^-\pi^0$, this decay can be constrained to the η mass but the final state contains the particle set $\eta : \{\pi^+\pi^-\gamma\gamma\}$ where the di-photon system can also be constrained to the π^0

mass, yielding a 2C fit. Since the reconstructed PFOs may be a superset of the true decay we have to choose secondary constraint particles from this set. This expands the total number of particle combinations that can be fitted, We can express these combinations with

$$C_{k,r,y}^{n,m,x} = \binom{n}{k}\binom{m}{r}\prod_{l=1}^{Z}\binom{x}{y} \tag{5.3}$$

where y is a set of particles chosen that satisfy the set required for the lth constraint. x is the available particles to choose from. For simplicity, x and y are mixtures of both charged and neutral particles. Here we require for constraints $l \epsilon 1 \ldots Z$ that $y \subset \{k, r\}$ and $x \subset \{n, m\}$. More explicitly, all combinations x of of the l-th constraint are generated from $n+m$ particles and chosen from this set is $k+r$ particles y. One way in which the combinatorics are reduced is that the particles for secondary constraints are required to be a subset of the particles that compose the parent generation. An additional problem is avoiding secondary mass constraints of the same generation that share the same final state particles. These combinations are produced but must not be fit, therefore, the combinatorics can be reduced by requiring no secondary particle subsets to intersect such that

$$y_i \not\cap y_j \quad \forall i \neq j \tag{5.4}$$

so, for all the mass constraints we apply, the masses are allowed to be the same since a particle may decay into multiples of the same particle, but the constituent particles of the final state may not have overlapping particle sets. That is, secondary constraints can not share the same particles. However, these set rules impose some limitations on the possible decays that can be addressed. Since secondary particles can not have overlapping sets, multi-generational decays (more than two) are not currently allowed because the parents from an earlier generation will share the same set of particles as its descendants that also decay. Therefore, to address this hierarchy problem, more extensive book-keeping is needed in relating particle relationships in a decay chain.

The secondary constraints implementation starts with two master arrays of neutral and charged

reconstructed particles. For 1C fitting the combinatoric fitting is addressed by constructing all array combinations of the indices of these particles. Secondary constraints also use array indices but with a special object, a struct massconstraint. The struct contains the mass, and an array of charged particle indices and an array of neutral particle indices. The indices contain a particlular particle combination that satisfies the secondary constraint. A massconstraint vector is constructed, to house each possible mass constraint. That is, each element of the constraint vector is one combination from $\binom{x}{y}$ for every constraint. Then, since more than one additional constraint is allowed, we have to choose a subset of constraints from the constraint vector for fitting. When choosing the set of constraints, the combination of constraints, and their combination of particles are checked for consistency with the set rules for x and y.

5.4 Parent Covariance Matrix Calculation

One of the useful outputs of the fit is the four-vector covariance matrix of the parent particle. The final covariance matrix is produced by a Jacobian transformation of the covariance matrix from the fit. The four-vector covariance matrix can be created for both the measured and fitted parameters. For some decay to arbitrary neutral, N, and charged particles C each with arbitrary parameterization $N(\xi_i)$, and $C(\xi_i)$. The covariance matrix V of this collection is represented by

$$V_{ij} = E[(\xi_i - \bar{\xi}_i)(\xi_j - \bar{\xi}_j)] \tag{5.5}$$

where V_{ij} is the expectation of the product of parameter deviations from the mean. The dimension of V_{ij} is dependent on the number of particles and the parameterization. For k neutral particles and r charged particles with η_n and η_c parameters respectively, then, the dimension of V_{ij} is $k\eta_n + r\eta_c$. To obtain the 4×4 four-vector matrix, V_f, a Jacobian transformation is used. Where V_f is given by

$$V_f = J^T V J \tag{5.6}$$

and the Jacobian J is denoted by

$$J = \begin{pmatrix} \frac{\partial P_x}{\partial \xi_0^{0_c}} & \cdots & \frac{\partial P_x}{\partial \xi_{\eta_c}^{0_c}} & \frac{\partial P_x}{\partial \xi_0^{r_c}} & \cdots & \frac{\partial P_x}{\partial \xi_{\eta_c}^{r_c}} & \frac{\partial P_x}{\partial \xi_0^{0_n}} & \cdots & \frac{\partial P_x}{\partial \xi_{\eta_n}^{k_n}} \\ \frac{\partial P_y}{\partial \xi_0^{0_c}} & & \ddots & & & & & & \\ \frac{\partial P_z}{\partial \xi_0^{0_c}} & & & \ddots & & & & & \\ \frac{\partial E}{\partial \xi_0^{0_c}} & & & & & & & & \end{pmatrix} \tag{5.7}$$

here the superscripts denote the rth and kth charged and neutral particles respectively, and the subscripts represent the parameters. Since the processor supports an arbitrary number of particle and constraints the necessary matrices are constructed in pieces. For the Jacobian, a submatrix for each particle is made, then all of the submatrices are concatenated together in a single matrix array by columns. In the code a submatrix is represented as:

$$j_i = \begin{pmatrix} \frac{\partial P_x}{\partial \xi_0} & \cdots & \frac{\partial P_x}{\partial \xi_{\eta_c}} \\ \frac{\partial P_y}{\partial \xi_0} & \cdots & \frac{\partial P_y}{\partial \xi_{\eta_c}} \\ \frac{\partial P_z}{\partial \xi_0} & \cdots & \frac{\partial P_z}{\partial \xi_{\eta_c}} \\ \frac{\partial E}{\partial \xi_0} & \cdots & \frac{\partial E}{\partial \xi_{\eta_c}} \end{pmatrix} \tag{5.8}$$

The code then joins each sub-matrix for each particle in a larger 2d array such that

$$\mathcal{M} = \bigcup_{i=1}^{N} j_i \tag{5.9}$$

But since the algebra requires a simple array by columns each Jacobian subset is parsed and η_c and η_n elements are extracted and placed such that they follow (5.7).

Chapter 6

Data Storage

The data structures that are stored for analysis consist of three main types: primitive, vectors, and 2D-vectors. Each piece of information is stored on a TTree and pre-formatted for post-fit analysis by a script that generates the proper classes to histogram all of the information. Pertinent values like fit probability, reconstructed energy, and fitted energy are stored in primitive (double) types for immediate access when plotting distributions. Parent particle information, such as fitted errors, or PDG codes are stored in 1D vectors. The rest of the information for each event for each particle, is stored in 2D vectors indexed by particle.

6.1 Data Structures

Again, some key values are stored as primitive types, and parent information is stored in vectors. But for the conglomerate of particles in each event, the four-vector parameters, the local parameters, the local parameterization errors are all stored in output. A pull distribution between the fit and measured quantities for every parameter is also stored in a structure that parallels the structure of the local parameterization. The pull distributions are given by

$$\frac{\xi_{fit} - \xi_{meas}}{\sqrt{\sigma^2_{meas} - \sigma^2_{fit}}} \tag{6.1}$$

Here the subscript fit denotes the post-fit parameter ξ_{fit} with post fit variance σ^2_{fit} and the $meas$ subscript denotes the pre-fit measured parameter ξ_{meas} with variance σ^2_{meas}. The parameters and

errors are stored for both fitted and measured quantities. The particles are separated into two groups, charged particles and neutral particles. The parameters for each particle are stored in sequence on a vector e.g. $\{\kappa, \theta, \phi\}$ then each vector is placed onto a vector, such that parameters are indexed by particle, which have consistent orders throughout every data structure.

6.2 Secondary Analysis

The secondary analysis is mostly automated. Histograms for every parameter for every particle in every data structure are created. The analysis uses workflow similar to what the TTree::MakeClass would generate. The program reads the output TTree from the constrained fitting processor using the TTreeReader from ROOT v6.08. The tree is parsed for variable names and a class containing ROOT histogram TH1D* objects is generated with every possible variable. The histograms are automatically initialized on the heap within the class constructor. The initial binning is an assumed $\sim 1\%$ statistics per bin, where the bounds are calculated from the minimum and maximum values of each parameter. The program also then automatically generates a script, Loop.cpp, that loops over every possible parameter and generates code to fill each parameter, link and instantiate the histogram class. The output script Loop.cpp can be run in the ROOT interpreter to create a new ROOT file with a well binned set of histograms. The quality of the binning and boundaries are subject to the quality of the cuts upstream in the processor. The intermediate histograms class was created as a quality control tool for fine tuning of finalized plots, as well as a basis for extending and creating additional plots relevant to the processed set of events.

Chapter 7

Results

Four data sets were generated in Pythia [14]. All are single particle decays produced without matrix elements. The decays considered are $J/\psi \to \mu^+\mu^-$, $\pi^0 \to \gamma\gamma$, $\eta \to \pi^+\pi^-\gamma$, and $\eta \to \pi^+\pi^-\pi^0$. Each data set is produced with a parent energy of 20 GeV, excluding the single pions, which are decayed at 10 GeV. The intrinsic widths of J/ψ and π^0 are approximated to 0 while the η decays' intrinsic width is consistent with the PDG value. Each sample of π^0s is allowed to decay inclusively. 10,000 events are generated per data set from Pythia in longform .hepevt files which are then converted to .stdhep using a java based .stdhep converter. The .stdhep files are fed to a GEANT4 based full simulation package called DDSim [15] which produces the detector response using the detector model ILD_l4_v02. The output of DDSim is read by the standard reconstruction with Pandora which creates the output LCIO. The output LCIO collections are then input through a pipeline of processors, including MCPfiltering, calibration, and the mass constraint fitter. An example of a single event in a $\eta \to \pi^+\pi^-\gamma$ decay is shown in Table 7.1.

The results of all of the mass constraint data sets are evaluated with a set of standard plots. The primary results are the reconstructed and fitted energy resolution of each parent decay, demonstrating the overall fit performance. A secondary assessment to the quality of the fitting, is the fit probability distribution. Since each decay event is independent, then any fit probability of any event is equally likely, thus the distribution of fit probability is expected to be uniform. The uniformity of the fit probability distribution serves as a metric to evaluate the particle selection hypothesis and single particle error estimation. Contribution to peaks at low fit probabilities are from improper characterization of errors, or improper child particle selection causing tails in the χ^2 distribution.

The tertiary insight to constraint and reconstruction performance is the rejected events. An event can be rejected for five reasons: (1) Not enough particles to satisfy the particle hypothesis (2) No fitted covariance matrix (the fit didn't converge properly) (3) Fit probability cut not met (4) ΔM Mass cut not met, where $\Delta M = |M_{meas} - M_g|$ (5) Fit converged, but somehow fit candidates are invalid or missing. However, the plots with rejected events exclude the fifth criteria because the frequency of (5) is less than 10 events per dataset.

To ensure that the fit is correctly working, the pull distributions between the fitted and measured parameters are shown to be consistent with a standard normal distribution, an example is given in Figure 7.1 and a table of all of the fitted parameters are given in Appendix A. All of the results shown are subject to calibration adjustments discussed in the next section.

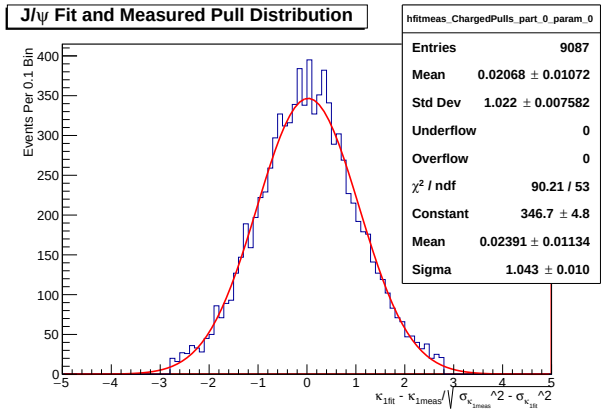

Figure 7.1: The J/ψ fit and measured pull distribution for the curvature κ_1 of a single track in an accepted event.

7.1 Calibration

The calibration processors were created to rescale poorly estimated parameters in the constrained fit. The calibrations are assessed using the characteristics of the pull distributions' pertinent parameters. For the charged particle track calibrations, 10,000 J/ψ decaying to di-muons were created in Pythia [14]. The pull distributions $\frac{\xi_{meas}-\xi_{gen}}{\sigma_{meas}}$between the measured muons and generator muons are analyzed in the MassConstraintFitter. The events that compose these distributions are required to pass the preliminary cuts in the MassConstraintFitter. The criteria to be a considered event is:

Table 7.1: Example event of a well measured decay of a 20 GeV $\eta \to \pi^+\pi^-\gamma$ with fit probability 0.988. The table shows the measured local parameters for each particle and the change in each parameter from the fit. The total energy from the reconstructed and fitted four-vector sum is also shown

Particle	E_{meas}[GeV] $\lvert\kappa_{meas}$ [GeV^{-1}]	θ_{meas} [rad]	ϕ_{meas} [rad]
γ	9.708 ± 0.56	2.03540 ± 0.00032	-2.32173 ± 0.00032
π^+	0.18718 ± 0.00019	2.07207 ± 0.00014	-2.34242 ± 0.00016
π^-	-0.25825 ± 0.00025	2.03612 ± 0.00019	-2.31868 ± 0.00021
Particle	E_{fit}[GeV] $\lvert\kappa_{fit}$ [GeV^{-1}]	θ_{fit} [rad]	ϕ_{fit} [rad]
γ	9.700 ± 0.10	2.03540 ± 0.00032	-2.32173 ± 0.00032
π^+	0.18718 ± 0.00019	2.07207 ± 0.00014	-2.34242 ± 0.00016
π^-	-0.25825 ± 0.00025	2.03612 ± 0.00019	-2.31868 ± 0.00021

Measured ηE [GeV]	Fit ηE [GeV]
20.137 ± 0.56	20.128 ± 0.10

we require the event to have two tracks, the invariant mass of the two track system has to be within 20 MeV of the J/ψ mass, and the constrained fit probability has to be greater than or equal to 0.5%. The particles that pass these cuts are matched with their generator particle from the filtered MCParticle collection. The matching is done based on an algorithm that compares each measured particle to every particle in the filtered MCParticle list. The particle that is considered a match has the smallest deviations in terms of the three local parameters, $(E|\kappa,\theta,\phi)$. It is possible for a chosen reconstructed particle to not be part of the initial decay; in this case there will be no true match with the filter MCParticle set. However, all particles are forced to match with a generator particle. This can cause some large deviations in the pull distributions. Such values are mitigated by fitting a standard normal distribution to the pull distributions. The following results in Figures 7.2, 7.3, and 7.4 are from J/ψ using the local parameterization (κ,θ,ϕ) where the pull distributions are displayed only containing one of the tracks from each accepted event.

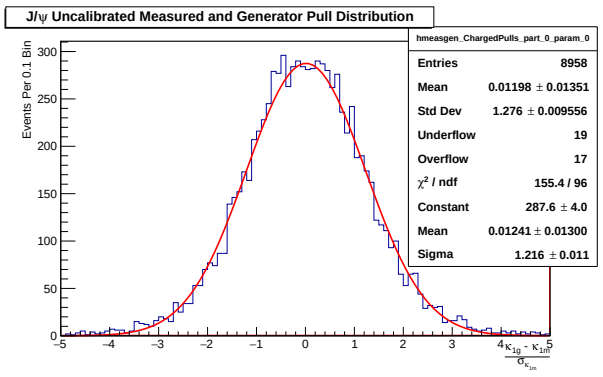

Figure 7.2: The gaussian fitted pull distribution between the inverse transverse momentum κ uncalibrated measurements and Monte Carlo values, normalized by the measured κ error σ_κ

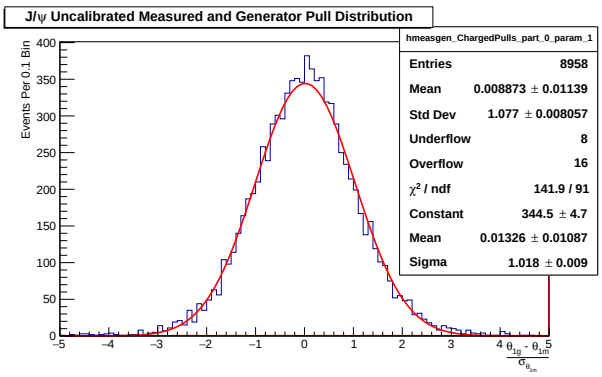

Figure 7.3: The gaussian fitted pull distribution between polar angles θ for the uncalibrated measurements and Monte Carlo values, normalized by the measured θ error σ_θ

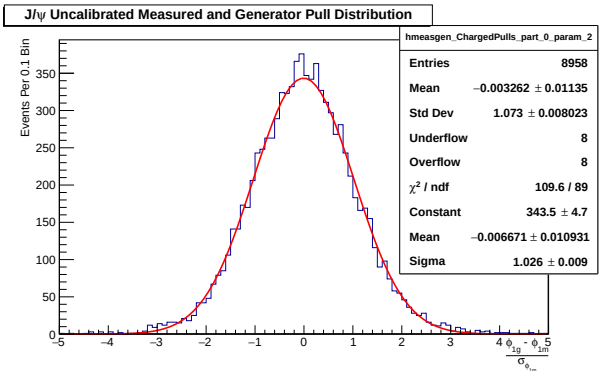

Figure 7.4: The gaussian fitted pull distribution between azimuthal angles ϕ for the uncalibrated measurements and Monte Carlo values, normalized by the measured ϕ error σ_ϕ.

The central limit theorem dictates that the pull distributions should be standard normal distributions centered on zero with unit variance. The angular distributions are consistent with $N(0,1)$, but the width of the κ distributions are too wide by 20%. This means that the current error is underestimated by this factor. The main track parameter corresponding to κ is the inverse radius of curvature Ω, so the error estimate for Ω is increased in the track calibration processor (along with adjusted covariance terms). The results are the three distributions in Figures 7.5, 7.6, and 7.7 consistent with a standard normal distribution. The error re-estimation also increases the fit probabilty of events in the χ^2 tail, resulting in better overall efficiency of events that pass the preliminary criteria.

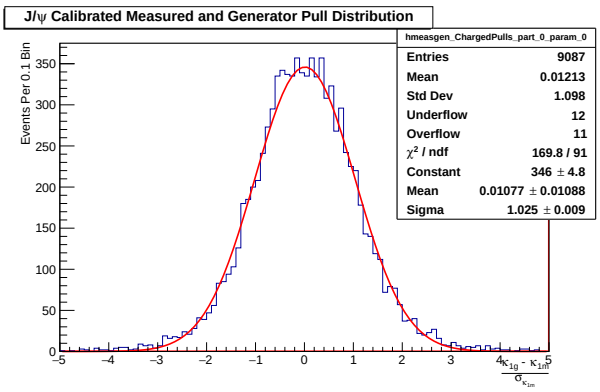

Figure 7.5: The gaussian fitted pull distribution between the inverse transverse momentum κ calibrated measurements and Monte Carlo values, normalized by the measured κ error σ_κ

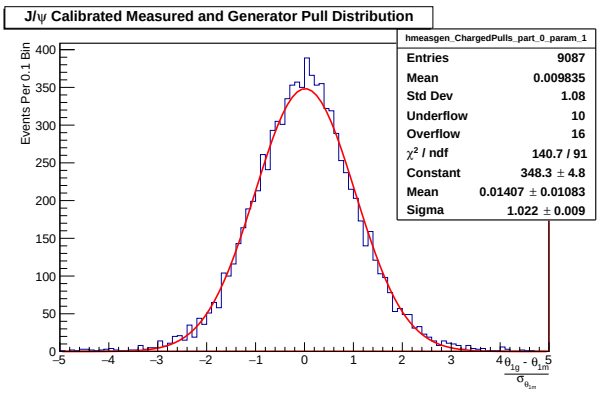

Figure 7.6: The gaussian fitted pull distribution between polar angles θ for the calibrated measurements and Monte Carlo values, normalized by the measured θ error σ_θ

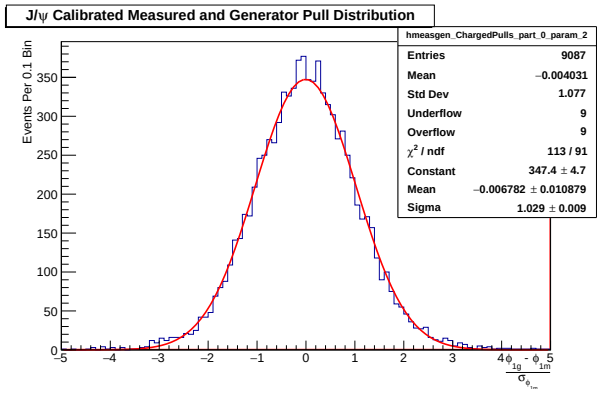

Figure 7.7: The gaussian fitted pull distribution between azimuthal angles ϕ for the uncalibrated measurements and Monte Carlo values, normalized by the measured ϕ error σ_ϕ.

The photon calibrations are performed by generating 10,000 10 GeV single photons uniform in ϕ and $\cos\theta$. The photons are run through the full simulation and standard reconstruction, using the same detector model as the muons. The photons pass through a two processor chain. The MCParticle collection is filtered by the MCParticleFilter, and the photon parameter distributions and pulls are produced in a PhotonChecks processor. The matching algorithm used for pairing is the same method used for pairing the di-muon particle sets. Since there is only a single photon in the Monte Carlo information, the "true" reconstructed photon is the particle closest to the generator photon in E, θ, ϕ. All events with multiple reconstructed photons are rejected. The pull distributions for the uncalibrated single photons are shown in Figures 7.8, 7.9, and 7.10.

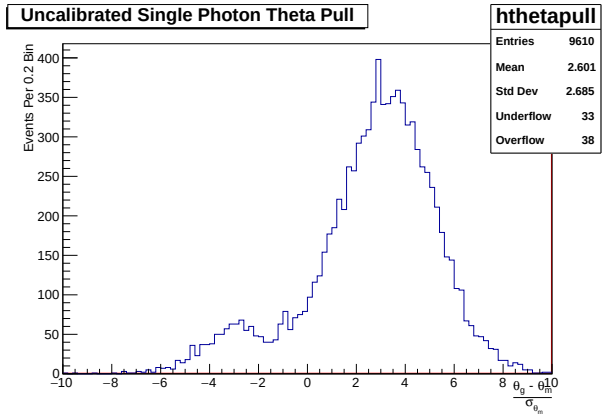

Figure 7.8: Single reconstructed photons polar angle θ pull distribution between the uncalibrated measurements and Monte Carlo values, normalized by the measured θ error σ_θ.

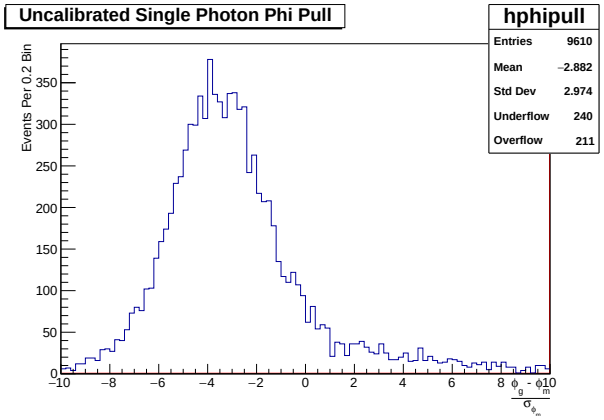

Figure 7.9: Single reconstructed photons azimuthal angle ϕ pull distribution between the uncalibrated measurements and Monte Carlo values, normalized by the measured ϕ error σ_ϕ.

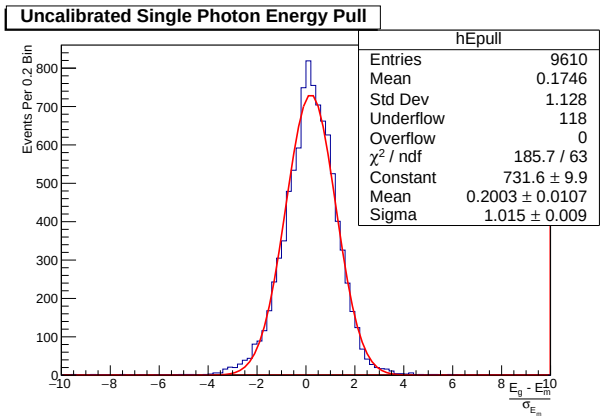

Figure 7.10: Single reconstructed photons energy, E, pull distribution between the uncalibrated measurements and Monte Carlo values, normalized by the measured ϕ error σ_ϕ.

The reconstructed energy resolution of a single photon from Figure 7.10 is adequate, but there is a significant bias in the angular reconstruction as shown in Figures 7.8 and 7.9. The bias is illustrated more explicitly in Figures 7.11 and 7.12 where the photon angular residuals between the reconstructed and generator angles are plotted as a function of the generator direction.

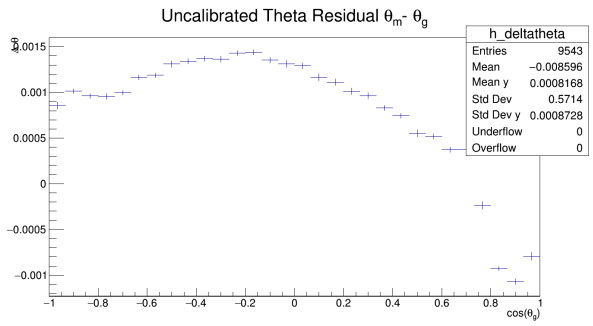

Figure 7.11: The θ residuals between the uncalibrated measurements and Monte Carlo values, plotted as a function of the cosine of the Monte Carlo polar angle.

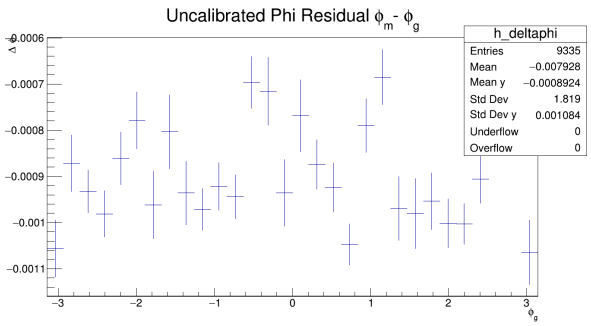

Figure 7.12: The ϕ residuals between the uncalibrated measurements and Monte Carlo values, plotted as a function of the Monte Carlo azimuthal angle.

To address the errors in photon angular reconstruction the angles of each photon are resimulated. Using the generator directions of the photons, new measured values of theta and phi are generated that are consistent with the proposed error model. This study has revealed a serious bug in the ILD ECAL simulation software that has been recently fixed, but whose fix was not available in time to incorporate in this work.

An additional photon data set is assessed to ensure the accuracy of the photon energy scale. 10,000 10 GeV π^0s were generated in Pythia. The π^0s are run through the full simulation, standard reconstruction, and mass constraint processor. The same detector models as the muons and photons are used. The calibrated and uncalibrated energy pull distributions are displayed in Figures 7.13, 7.14 which only contain a single photon from the di-photon decay products of each event. The reconstructed angles for the uncalibrated pions are resimulated, so the angular pull distributions are nearly idealized.

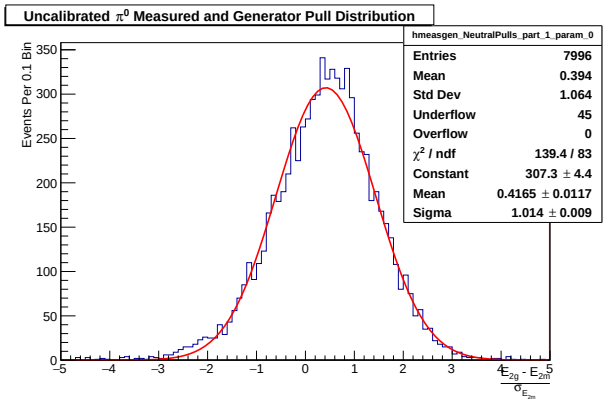

Figure 7.13: π^0 Energy pull distribution between the uncalibrated measurements and Monte Carlo values, normalized by the measured energy error σ_E.

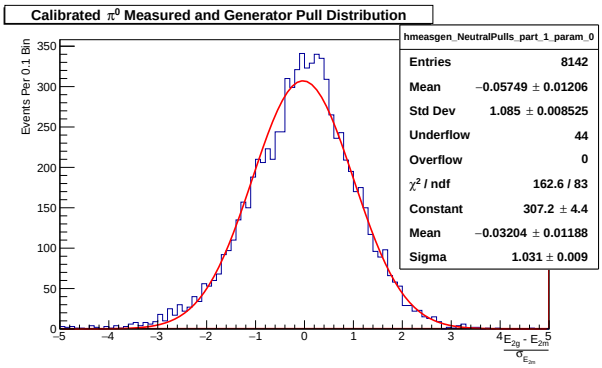

Figure 7.14: π^0 Energy pull distribution between the calibrated measurements and Monte Carlo values, normalized by the calibrated measured energy error σ_E.

The reconstructed energy for the di-photon system is still subject to a significant bias. The photon energy is overestimated by $\sim 5\%$. Reducing the measured photon energy centers the energy pull distribution closer to the ideal value as shown in Figure 7.14. However, performing the calibration based on the accepted events subject to the mass constraint cuts does not necessarily guarantee unbiased results. The calibration factor is chosen based on the energy correction of the events that pass the preliminary cuts for the constrained fit.

The differing energy resolution behavior between 10 GeV single photons and 10 GeV single pions from Figures 7.10 and 7.13 demonstrates a need for more careful event specific photon calibrations. The energy differences could be due to, most likely, photon energy scale, or, potentially photon shower profiles. The quick fixes in the photon energies and angles are applied specifically to the more complicated data sets to demonstrate the benefit of the mass constraint. A more involved treatment of photon energy would be sensitive to energy scale.

7.2 $J/\psi \rightarrow \mu^+\mu^-$

The J/ψ decay to di-muons is an ideal event for mass constraints, the intrinsic mass resolution of the J/ψ is very narrow and the decay products are easily identified, reconstructed, and have good resolution. The muons also have minimal interaction with the detector and often do not produce photons or other particles that can degrade reconstruction. This event is a good calibration tool to

test the error models for charged tracks, examine the impact of mass constraints on charged tracks, and serve as a general use-case for only charged particles in the processor.

The mass constraints were applied by extracting two tracks from each event for 10,000 events. The muon mass was applied to each track and the constraint applied was the J/ψ mass of 3.096916 GeV. The mass constrained fit is accepted if the reconstructed mass of the tracks are within 0.02 GeV of the J/ψ mass and the probability of the fit $P_{fit} > 0.5\%$

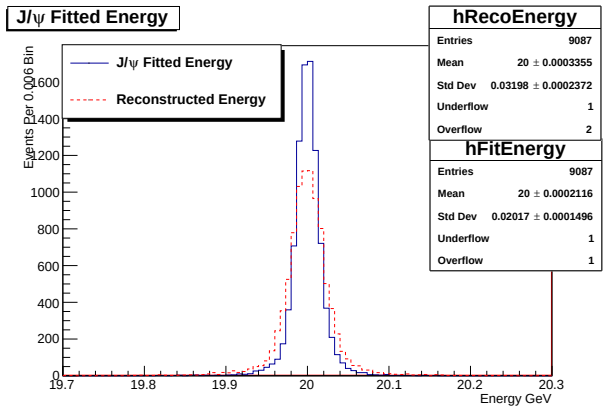

Figure 7.15: The reconstructed and fitted energies of J/ψ two track mass constraint candidates.

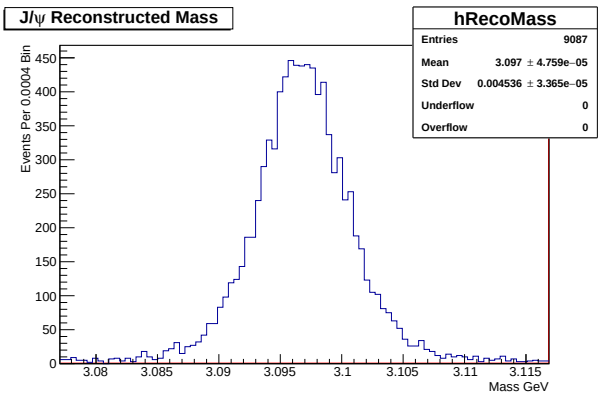

Figure 7.16: The reconstructed mass of the mass constraint candidate with a two muon track final state.

Even though the reconstruction of the J/ψ muons is nearly ideal, there is still a reasonable improvement in the overall energy reconstruction of the J/ψ. The narrowness of the intrinsic width of the J/ψ also serves as an ideal candidate for application of mass constraints. The reconstructed mass distribution in Figure 7.16 collapses into a delta function with the imposed mass constraint, and as a consequence, the reconstructed parent energy width in 7.15 is reduced by a factor of 0.63. The J/ψ events have the highest efficiency for all the data sets with 90.87% of events passing the acceptance requirements. Events that are rejected in Figure 7.17 are likely rejected due to asymmetry in decay energies such that one track is not reconstructed, or not well reconstructed, or, the track goes down the beam pipe. Figure 7.18 demonstrates the energy resolution as a function of the J/ψ polar angle, the energy resolution degrades as the tracks approach a more longitudinal orientation. The tracks that cause the most degraded parent energy resolution also have least transverse momentum and largest error.

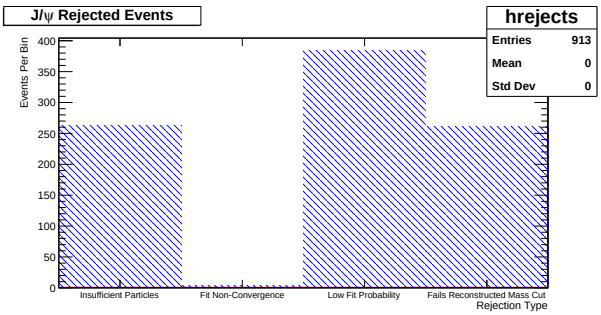

Figure 7.17: The rejected instances of J/ψ events that did not become mass constraint candidates.

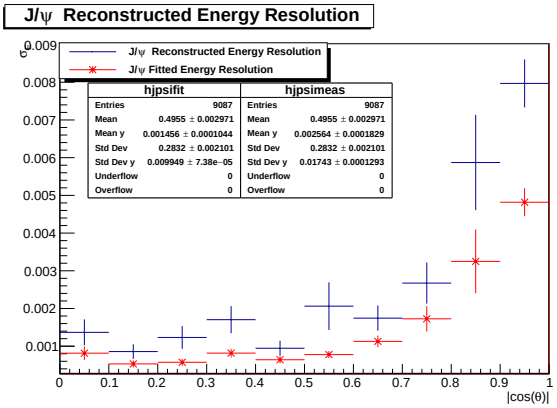

Figure 7.18: The J/ψ mass constraint candidates measured and fitted energy resolution as a function of the absolute cosine of the polar angle of the reconstructed J/ψ

7.3 $\pi^0 \rightarrow \gamma\gamma$

The π^0 decay serves as a use case for the processor working with no charged particles and as a calibration tool for photons. 10,000 10 GeV π^0's were produced which decayed inclusively. The candidates for mass constraints contained two photons. The di-photon system was constrained to a mass of 0.1349766 GeV. The allowed deviation from the true mass is 0.05 GeV and the minimum fit probability allowed is $P_{fit} > 0.5\%$.

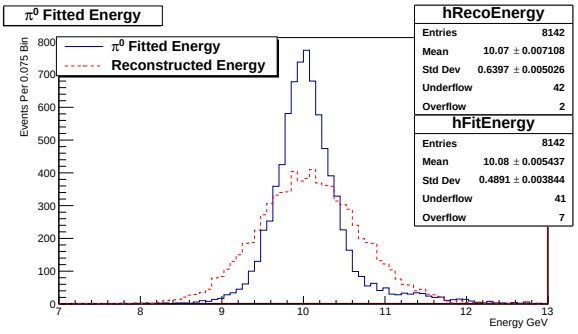

Figure 7.19: The reconstructed and fitted energies of π^0 two photon mass constraint candidates.

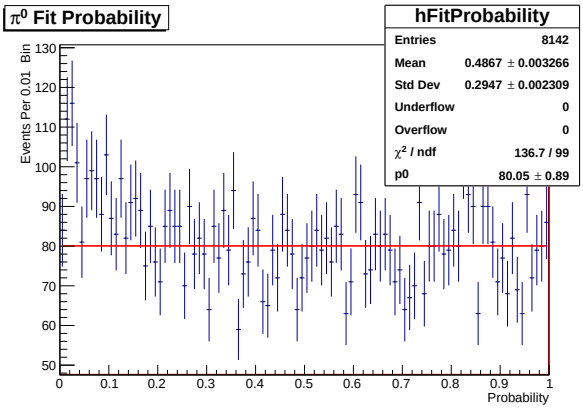

Figure 7.20: The χ^2 fit probability distribution of π^0 mass constraint candidates.

The benefit to the overall energy resolution is significant and is evident from Figure 7.19.

The mean of the fitted parent energy distribution is shifted away from the true value by moving from 10.07 GeV to 10.08 GeV. This increasing energy bias is likely due to the photon energy reconstruction problems, which are not as finely calibrated based on energy scale as they should be. The events that are rejected in Figure 7.21 are most likely due to asymmetric photon energies, such that, one small photon cluster is either not reconstructed or merged with the higher energy cluster. The overall π^0 energy resolution as a function of the maximum photon energy in Figure 7.22 shows that in the ideal case of two lowest possible energy photons decreases the π^0 fractional energy resolution from $\sim 18\%/\sqrt{E}$ to $\sim 6\%/\sqrt{E}$. Thus, the energy asymmetry of the photon dramatically affects the performance of the constrained fitting. When a single photon takes up most of the energy of the π^0 decay the effect of the mass constraint fit is nearly lost. It is also likely that in many of these types of events the most energetic photon produces a secondary clusters that are considred as a second photon. These secondaries could be paired with the energetic photon, while the true partner to the energetic photon is lost in the reconstruction. A possible cause for the low fit probability in Figure 7.20 could be these mismatched photons.

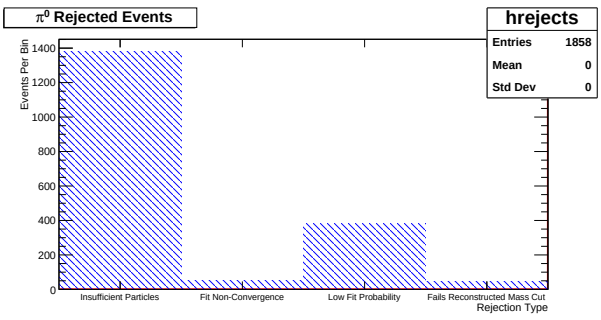

Figure 7.21: The rejected instances of π^0 events that did not become mass constraint candidates.

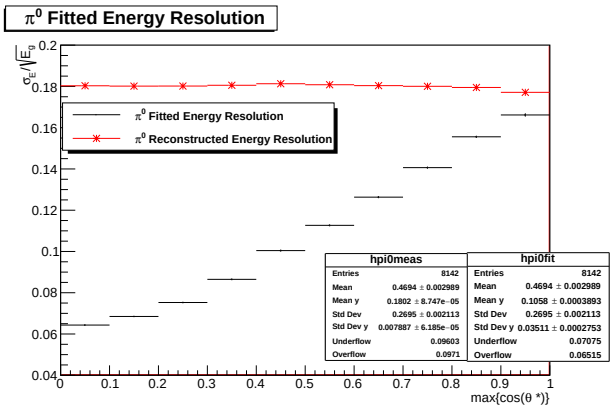

Figure 7.22: The reconstructed and fitted π^0 energy resolution. Plotted as a function of the max $\cos\theta^*$ where θ^* is the angle between a photon and the π^0 boost direction in the CM frame.

7.4 $\eta \to \pi^+\pi^-\gamma$

The $\eta \to \pi^+\pi^-\gamma$ seems to be the ideal case for the mass constraints, and the simplest combination of neutral and charged particles. 10,000 20 GeV η's were produced decaying exclusively to $\pi^+\pi^-\gamma$.

The candidate events for mass constraints contained two charged tracks and one photon. The system is constrained to 0.547862 GeV. The allowed reconstructed mass deviation from the true mass was 0.15 GeV and the minimum fit probability allowed was 0.5%

The energy resolution benefit in Figure 7.23 was the best improvement in all of the data sets with a parent energy width reduction by a factor of 0.54. The rejected events in Figure 7.25 are due to two main reasons: improperly resolved photons, and low fit probabilities. The fit probabilities that fall below the acceptance criteria and low fit probability peak in Figure 7.24 are likely influenced by lost photons that are replaced by photons created from the pions interactions with the detector, or pion tracks that are longitudinally oriented. The failure to reconstruct the parent decay's photon is illustrated by the η photon energy distribution in Figure 7.27 which shows that high energy photons are less frequent in the decay and that the two pions tend to take most of the energy in the system. Also, plotting the energy resolution as a function of photon energy, i.e. photon CM boost axis angle seen in Figure 7.26, the greatest benefit is at low photon energies (which is fortunately more common) . At these photon energies the information from the tracks and the constraint can best benefit the overall resolution.

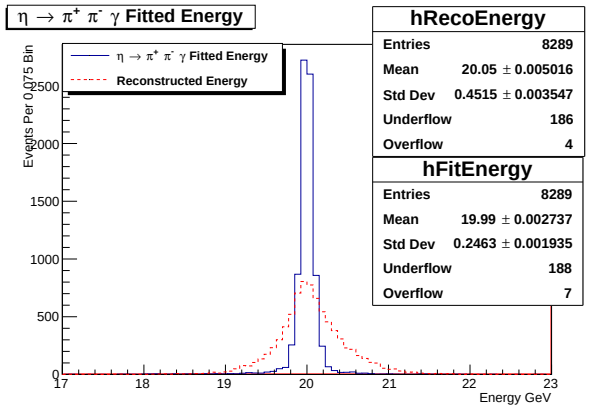

Figure 7.23: The reconstructed and fitted energies of $\eta \to \pi^+\pi^-\gamma$ mass constraint candidates.

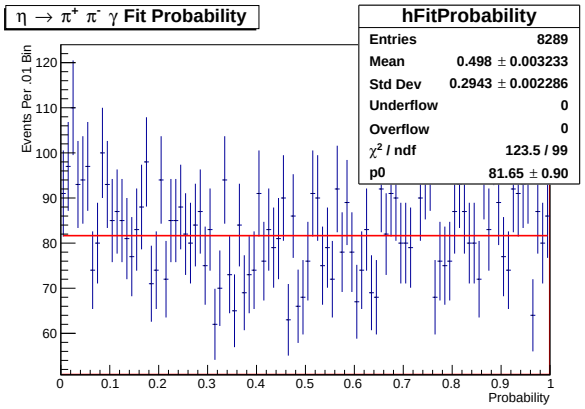

Figure 7.24: The χ^2 fit probability distribution of $\eta \to \pi^+\pi^-\gamma$ mass constraint candidates.

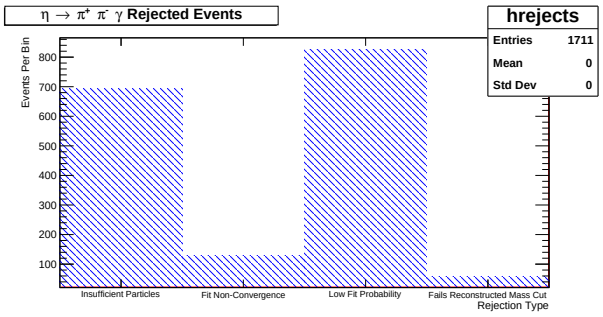

Figure 7.25: The rejected instances of $\eta \to \pi^+\pi^-\gamma$ events that did not become mass constraint candidates.

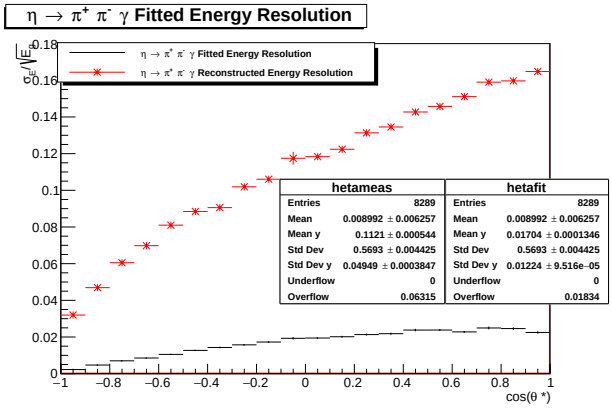

Figure 7.26: The reconstructed and fitted $\eta \to \pi^+\pi^-\gamma$ energy resolution. Plotted as a function of $\cos\theta^*$ where θ^* is the angle between a photon and the η boost direction in the CM frame. The y-axis scale is chosen to show the overall dependence and improvement in photon resolution.

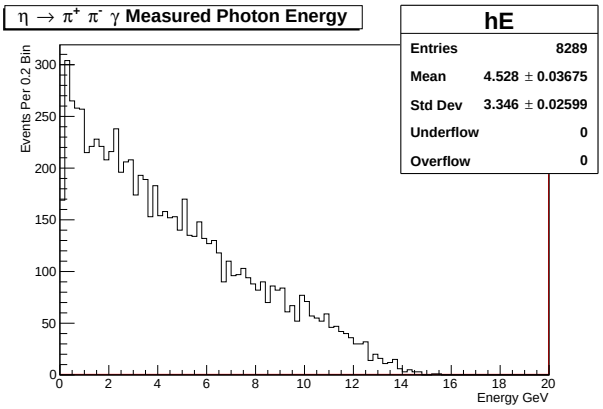

Figure 7.27: The Energy distribution of the single photon in the $\eta \to \pi^+\pi^-\gamma$ events.

7.5 $\eta \to \pi^+\pi^-\pi^0$ 1C

The single constraint for the $\eta \to \pi^+\pi^-\pi^0$ decay is used to test the processor on a more complex decay topology with a mixture of neutral and charged particles. The performance of 1C and 2C fits are compared to illustrate the benefit of fitting with multiple constraints. 10,000 20 GeV η's are produced decaying exclusively, with π^0's that decay inclusively. The four particle final state is constrained to 0.547862 GeV. The allowed mass deviation from the true mass is 0.15 GeV and the minimum fit probability allowed is $P_{fit} > 0.5\%$.

The performance for a single constraint is not as good as $\pi^+\pi^-\gamma$ because of the additional photon

in the system as shown in Figure 7.28 which only has a reduction factor of 0.82 of the parent energy resolution. The π^0 can also decay asymmetrically which makes the reconstruction of two separate photons more difficult in the presence of other particles. The fit probability distribution in Figure 7.29 and the rejected events in Figure 7.30 are similar to the distributions of the single π^0 data set with the exception of the energy resolution enhancement in Figure 7.31. The energy resolution as a function of the π^0 energy is nearly constant for all π^0 energies, so, contrary to the higher photon energies degrading energy resolution enhancement in Figure 7.22 the tracks in the system compensate for the loss in resolution. The efficiency is also lower than all of the other previous data sets. The probability to reconstruct a π^0 given the acceptance cuts is $\sim 80\%$ and the probability to reconstruct two tracks is $\sim 90\%$, thus the probability to reconstruct two tracks and a π^0 is $\sim 70\%$. Therefore, the 1C efficiency is as good as it could possibly be.

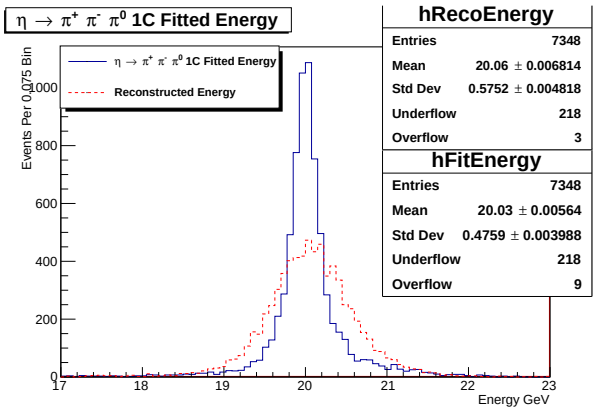

Figure 7.28: The reconstructed and fitted energies of $\eta \to \pi^+\pi^-\pi^0$ 1C mass constraint candidates.

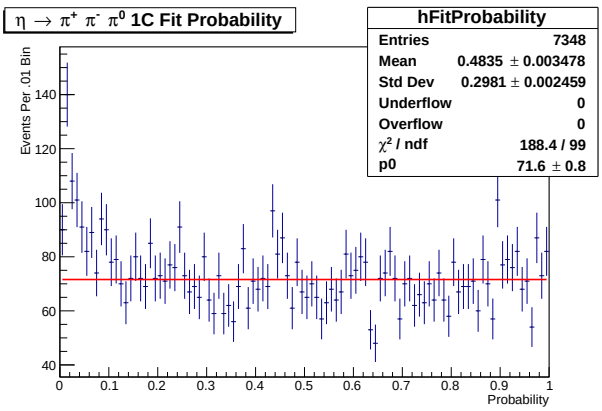

Figure 7.29: The χ^2 fit probability distribution of $\eta \to \pi^+\pi^-\pi^0$ 1C mass constraint candidates.

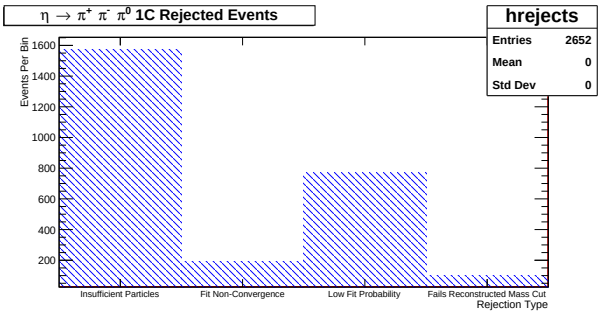

Figure 7.30: The rejected instances of $\eta \to \pi^+\pi^-\pi^0$ 1C events that did not become mass constraint candidates.

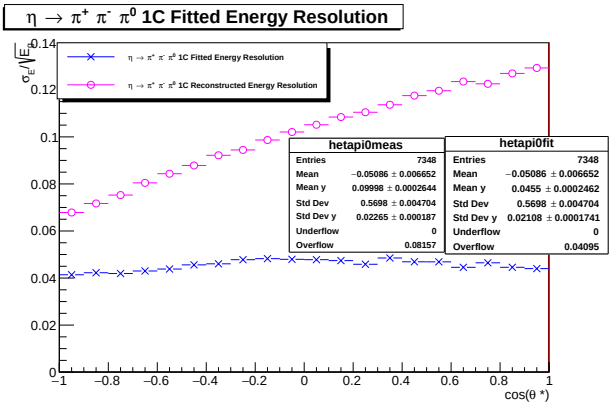

Figure 7.31: The reconstructed and fitted $\eta \to \pi^+\pi^-\pi^0$ energy resolution for the single η mass constraint. Plotted as a function of $\cos\theta^*$ where θ^* is the angle between the π^0 and the η boost direction in the CM frame. The y-axis scale is chosen to show the overall dependence and improvement in photon resolution.

7.6 $\eta \to \pi^+\pi^-\pi^0$ 2C

The double constraint shows the benefit of multiple constraints on more complicated decay topologies. 10,000 20 GeV η's are produced decaying in the same fashion as the 1C fit, the only difference is that the di-photon system is constrained to the π^0 mass 0.1349766 GeV. All of the acceptance cuts are identical to the 1C fit.

The overall performance of the 2C fit was much better than the 1C fit with evidence from Figure 7.32. The reduction in the parent energy width is enhanced from 0.82 → 0.65 by adding an additional constraint. The efficiency was lower because the additional mass constraint weeds out the particle combinations that coincidentally mimic the true final state particles. Imposing the additional mass constraint forces the fake events to have low fit probabilities, which are inevitably rejected as shown in Figure 7.33 by contrasting the 1C and 2C rejected events. The efficiency is also reasonable when considering the probability of track and π^0 reconstruction like in the 1C fit. The performance as a function of π^0 energy as in Figure 7.34 is very good, and nearly a factor of 2 better than the 1C fit. There is also an increase in performance in $\cos(\theta^*) > 0.4$ which requires further investigation.

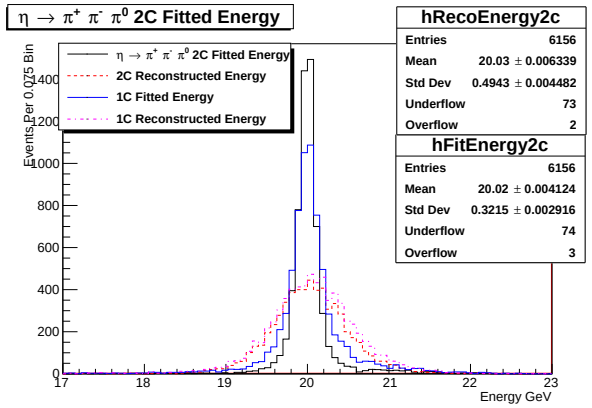

Figure 7.32: The reconstructed and fitted energies of $\eta \to \pi^+\pi^-\pi^0$ 2C mass constraint candidates superimposed on the 1C mass constraint reconstructed and fitted energies.

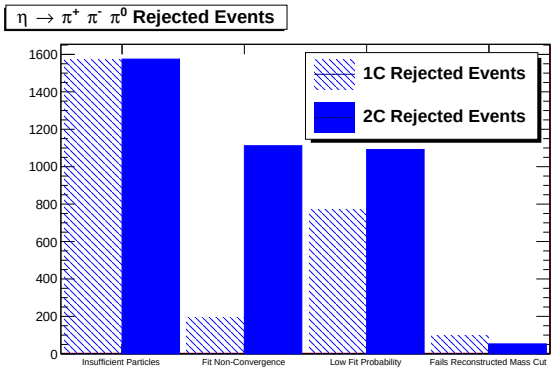

Figure 7.33: The rejected instances of $\eta \to \pi^+\pi^-\pi^0$ 1C and 2C events that did not become mass constraint candidates.

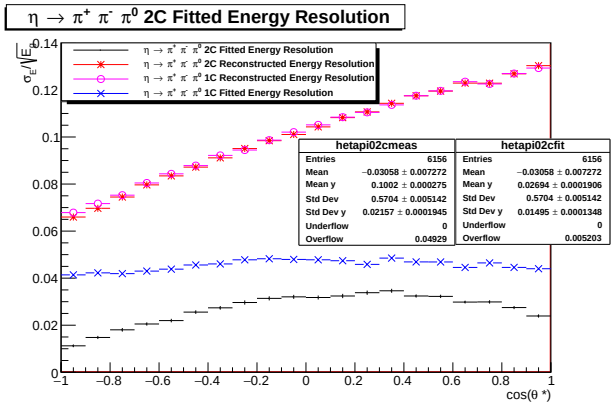

Figure 7.34: The reconstructed and fitted $\eta \to \pi^+\pi^-\pi^0$ energy resolution for the 1C and 2C mass constraints. Plotted as a function of $\cos\theta^*$ where $\theta*$ is the angle between the π^0 and the η boost direction in the CM frame. The y-axis scale is chosen to show the overall dependence and improvement in photon resolution.

7.7 Conclusion

Table 7.3: Collection of all of the reconstructed and fitted energy statistics. The σ values shown are the sample standard deviations from the mass constraint candidate energy distributions. The ratio of the widths and the sample mean fitted and reconstructed energies are also shown.

Decay Mode	σ_{fit} [GeV]	σ_{meas} [GeV]	$\sigma_{fit}/\sigma_{meas}$
$J/\psi \to \mu^+\mu^-$	0.02017 ± 0.00015	0.03198 ± 0.00024	0.63
$\pi^0 \to \gamma\gamma$	0.4891 ± 0.0038	0.6397 ± 0.0050	0.76
$\eta \to \pi^+\pi^-\gamma$	0.2463 ± 0.0019	0.4515 ± 0.0035	0.54
$\eta \to \pi^+\pi^-\pi^0$ 1C	0.4759 ± 0.0040	0.5752 ± 0.0048	0.82
$\eta \to \pi^+\pi^-\pi^0$ 2C	0.3215 ± 0.0029	0.4943 ± 0.0045	0.65

Decay Mode	E_{fit} [GeV]	E_{meas} [GeV]
$J/\psi \to \mu^+\mu^-$	20.00000 ± 0.00021	20.00000 ± 0.00034
$\pi^0 \to \gamma\gamma$	10.0800 ± 0.0054	10.0700 ± 0.0071
$\eta \to \pi^+\pi^-\gamma$	19.9900 ± 0.0027	20.0500 ± 0.0050
$\eta \to \pi^+\pi^-\pi^0$ 1C	20.0300 ± 0.0056	20.0600 ± 0.0068
$\eta \to \pi^+\pi^-\pi^0$ 2C	20.0200 ± 0.0041	20.0300 ± 0.0063

The application of mass constraints to different sets of particles proves to be a useful tool. Table 7.3 shows that every type of event considered showed improvement in the overall energy resolution of the system. The photon energy scale needs to be better addressed to guarantee beneficial results. Also, the re-simulation of the photon direction and use of a perfect Monte Carlo error

model for the angles yields idealized results. With less accurate angles the events with photons could have slightly less accurate fit estimates for the photon energy. Since the photon energy resolution dominates the overall error, the precision measurements from the tracks and photon angles contribute significantly in the photon energy adjustment and shift the value towards the true energy. High photon multiplicity degrades resolution on the parent particle as a function of the number of photons. But, it is possible to mitigate this degradation by the application of multiple constraints on a system. This eliminates background events that coincidentally imitate the correct final state particles and further improves the overall energy resolution of the system. In order to gain more improvement on the energy resolution, more constraints could be added to the system, such as vertex constraints, that is, requiring tracks and neutral particles, with a common parent, to come from a common vertex. With additional improvements to energy measurement, a possible channel to perform precision measurements would be visible hadronic Higgs decays with low photon multiplicity.

Appendices

Appendix A

Table of fit and measured parameter pull distributions

Below is a collection of all of the pull distributions between the measured and fitted values of every local parameter of the charged and neutral particles. The list corresponds to Gaussian fits for each particle in every data set provided. The pull distribution is defined as in equation 6.1

Decay	Particle i Parameter	Fitted μ	Fitted σ
$J/\psi \to \mu^+\mu^-$	κ_1	0.03 ± 0.01	1.03 ± 0.01
	θ_1	-0.01 ± 0.01	1.03 ± 0.01
	ϕ_1	-0.002 ± 0.01	1.03 ± 0.01
	κ_2	-0.02 ± 0.01	1.03 ± 0.01
	θ_2	0.002 ± 0.01	1.02 ± 0.01
	ϕ_2	0.004 ± 0.01	1.03 ± 0.01
$\pi^0 \to \gamma\gamma$	E_1	-0.08 ± 0.01	1.05 ± 0.01
	θ_1	-0.03 ± 0.01	1.05 ± 0.01
	ϕ_1	-0.02 ± 0.01	1.05 ± 0.01
	E_2	-0.08 ± 0.01	1.05 ± 0.01

	θ_2	0.03 ± 0.01	1.05 ± 0.01
	ϕ_2	0.02 ± 0.01	1.05 ± 0.01
$\eta \to \pi^+\pi^-\gamma$	κ_1	0.03 ± 0.01	1.03 ± 0.01
	θ_1	-0.01 ± 0.01	1.02 ± 0.01
	ϕ_1	0.002 ± 0.01	1.04 ± 0.01
	κ_2	-0.01 ± 0.01	1.03 ± 0.01
	θ_2	-0.01 ± 0.01	1.01 ± 0.01
	ϕ_2	-0.01 ± 0.01	1.04 ± 0.01
	E_1	0.13 ± 0.01	1.03 ± 0.01
	θ_1	-0.01 ± 0.01	1.04 ± 0.01
	ϕ_1	0.01 ± 0.01	1.04 ± 0.01
$\eta \to \pi^+\pi^-\pi^0$ 1C	κ_1	0.01 ± 0.01	1.05 ± 0.01
	θ_1	0.02 ± 0.01	1.09 ± 0.01
	ϕ_1	0.001 ± 0.01	1.09 ± 0.01
	κ_2	-0.002 ± 0.01	1.04 ± 0.01
	θ_2	-0.01 ± 0.01	1.01 ± 0.01
	ϕ_2	0.02 ± 0.01	1.01 ± 0.01
	E_1	0.04 ± 0.01	1.09 ± 0.01

	θ_1	-0.02 ± 0.01	1.10 ± 0.01
	ϕ_1	0.02 ± 0.01	1.10 ± 0.01
	E_2	0.04 ± 0.01	1.09 ± 0.01
	θ_2	-0.01 ± 0.01	1.10 ± 0.01
	ϕ_2	-0.01 ± 0.01	1.10 ± 0.01
$\eta \to \pi^+\pi^-\pi^0$ 2C	κ_1	-0.01 ± 0.01	1.01 ± 0.01
	θ_1	0.02 ± 0.01	1.01 ± 0.01
	ϕ_1	-0.01 ± 0.01	1.02 ± 0.01
	κ_2	-0.01 ± 0.01	1.02 ± 0.01
	θ_2	-0.01 ± 0.01	1.02 ± 0.01
	ϕ_2	-0.01 ± 0.01	1.02 ± 0.01
	E_1	-0.01 ± 0.01	0.99 ± 0.01
	θ_1	-0.01 ± 0.01	1.01 ± 0.01
	ϕ_1	0.01 ± 0.01	1.02 ± 0.01
	E_2	-0.04 ± 0.01	1.04 ± 0.01
	θ_2	-0.004 ± 0.01	1.03 ± 0.01
	ϕ_2	-0.01 ± 0.01	1.04 ± 0.01

Appendix B

Description of XML parameters

Each processor uses an input XML file that contains all of the relevant parameters associated to each unique run. The required parameters and their description is listed below

MCParticleFilter Parameters	Description
MCParticleCollection	The string for the LCIO::MCParticle collection used for input
OutputParticleCollectionName	The string for the LCIO::MCParticle collection subset being created for output
Printing	The standard output printing verbosity

PhotonCalibration Parameters	Description
InputParticleCollectionName	The string for the LCIO::ReconstructedParticle collection used for input

OutputParticleCollectionName	The string for the LCIO::ReconstructedParticle collection subset being created for output
MCParticleCollection	The string for the LCIO::MCParticle collection used for input
CheatAngles	The boolean option to re simulate photon angles
dTheta	Normal error [mrad] for generating new photon θ values
dPhi	Normal error [mrad] for generating new photon ϕ values
EnergyCalibration	Calibration scale factor for photon energy E
Printing	The standard output printing verbosity

TrackCalibration Parameters	Description
InputTrackCollectionName	The string for the LCIO::Track collection used for input
OutputTrackCollectionName	The string for the LCIO::Track collection being created for output
D0ErrCalibration	Calibration factor for the error of the helix impact parameter d_0

Z0ErrCalibration	Calibration factor for the error of the helix impact parameter $z0$
OmeErrCalibration	Calibration factor for the error of the signed inverse track curvature Ω
PhiErrCalibration	Calibration factor for the error of the azimuthal orientation of the track ϕ_0
TanLErrCalibration	Calibration factor for the error of the polar orientation of the track $\tan\lambda$
Printing	The standard output printing verbosity

MassConstraintFitter Parameters	Description
RootFileName	Name of the output .root file containing the pertinent parameter TTree
InputParticleCollectionName	The string for the LCIO::ReconstructedParticle collection used for input
InputTrackCollectionName	The string for the LCIO::Track collection used for input
MCParticlesColletion	The string for the LCIO::MCParticle collection used for input
Printing	The standard output printing verbosity

parentPdg	The PDG code for the parent particle
parentMass	The parent mass [GeV]
parentCharge	Integer charge of the parent particle
nDaughters	The number of particles produced in the initial decay of the parent
nCharged	The number of charged particles produced in the initial decay of the parent
nNeutral	The number of neutral particles produced in the initial decay of the parent
nChargedParams	The number of parameters used in the local parameterization of the charged particles
nNeutralParams	The number of parameters used in the local parameterization of the neutral particles
daughterChargedPdgs	An integer vector of PDG codes for the charged particles in the initial decay
daughterNeutralPdgs	An integer vector of PDG codes for the neutral particles in the initial decay
daughterChargedMass	A float vector of the charged particle masses [GeV] of the initial decay
daughterNeutralMass	A float vector of the neutral particle masses [GeV] of the initial decay

FitProbabilityCut	The minimum value allowed for χ^2 fit probability
AllowedMassDeviation	The allowed mass deviation of the set of reconstructed particles from the parent mass
FitAnalysis	Boolean option for constructing fit analysis root file, 0 =No 1 =Yes
GeneratorAnalysis	Boolean option for doing fit analysis with MCParticle information, 0 =No 1 =Yes
nMassConstraints	The number of mass constraints being applied to the final state particles
SecondaryMasses	A float vector of the masses [GeV] for all the secondary mass constraints
SecondaryNCharged	An integer vector for the number of neutral particles in each secondary constraint
SecondaryNNeutral	An integer vector for the number of charged particles in each secondary constraint

Appendix C

Example steering file

```
<marlin>
 <execute>
   <processor name="MyPhotonCalibration" />
   <processor name="MyTrackCalibration" />
   <processor name="MyMCParticleFilter" />
   <processor name="MyMassConstraintFitter"/>
   <processor name="MyLCIOOutputProcessor"/>
 </execute>

 <global>
   <parameter name="LCIOInputFiles"> ../slciofiles/Eta_pi0_20GeV_REC.slcio
       </parameter>
   <parameter name="SkipNEvents" value="0" />
   <parameter name="MaxRecordNumber" value="0" /> <!  0 is all events  >
   <parameter name="SupressCheck" value="false" />
   <parameter name="GearXMLFile" value="gear_ILD_l4_v02_dd4hep.xml" />
   <parameter name="Verbosity"
       options="DEBUG0 4 ,MESSAGE0 4 ,WARNING0 4 ,ERROR0 4 ,SILENT">
   DEBUG </parameter>
 </global>

  <processor name ="MyPhotonCalibration" type="PhotonCalibration">
   <parameter name="InputParticleCollectionName" value="PandoraPFOs" />
   <parameter name="OutputParticleCollectionName" value="CalibratedPhotons" />
   <parameter name="EnergyCalibration" value="0.95" />
```

```
   <parameter name="Printing" value="5" />
 <!  direction cheating parameters  >
   <parameter name="MCParticlesCollection" type="string"
       lcioInType="MCParticle">
     MCParticle </parameter>
   <parameter name="CheatAngles" value="1" />
   <parameter name="dTheta" value=".001"/>
   <parameter name="dPhi" value=".001"/>
   <parameter name="AllowedEnergyDeviation" value="999"/>
   <parameter name="AllowedThetaDeviation" value="999"/>
   <parameter name="AllowedPhiDeviation" value="999"/>
</processor>

  <processor name="MyTrackCalibration" type="TrackCalibration">
  <parameter name="InputTrackCollectionName" value="MarlinTrkTracks" />
  <parameter name="OutputParticleCollectionName" value="CalibratedTracks" />
  <parameter name="D0ErrCalibration" value="1.0" />
  <parameter name="Z0ErrCalibration" value="1.0" />
  <parameter name="OmeErrCalibration" value="1.20" />
  <parameter name="PhiErrCalibration" value="1.0" />
  <parameter name="TanLErrCalibration" value="1.0" />
  <parameter name="Printing" value="5" />
 </processor>

 <processor name="MyMCParticleFilter" type="MCParticleFilter">
  <parameter name="MCParticlesCollection" type="string"
      lcioInType="MCParticle">
  MCParticle </parameter>
  <parameter name="OutputParticleCollectionName" value="MCDecayParticles" />
  <parameter name="Printing" value="5" />
 </processor>

 <processor name="MyMassConstraintFitter" type="MassConstraintFitter">
```

```
    <parameter name="MCParticleCollection" type="string"
        lcioInType="MCParticle">
     MCDecayParticles </parameter>
    <parameter name="Printing" value="5" />
    <parameter name="RootFile" value="MassConstraint2C_calibrated.root" />
    <parameter name="parentPdg" value="221" />
    <parameter name="parentMass" value="0.547862" />
    <parameter name="parentCharge" value="0" />
    <parameter name="nDaughters" value="4" />
    <parameter name="nCharged" value="2" />
    <parameter name="nNeutral" value="2" />
    <parameter name="nNeutralParams" value="3" />
    <parameter name="nChargedParams" value="3" />
    <parameter name="daughterChargedPdgs" type="IntVec"> 211 </parameter>
    <parameter name="daughterNeutralPdgs" type="IntVec"> 22 </parameter>
    <parameter name="daughterChargedMass" type="FloatVec"> 0.13957018
        </parameter>
    <parameter name="daughterNeutralMass" type="FloatVec"> 0.0 </parameter>
    <parameter name="InputParticleCollectionName" value="CalibratedPhotons" />
    <parameter name="InputTrackCollectionName" value="CalibratedTracks" />
    <parameter name="FitProbabilityCut" value="0.005" />
    <parameter name="AllowedMassDeviation" value="0.15" />
    <parameter name="fitter" value="0" />
    <parameter name="FitAnalysis" value="1" />
    <parameter name="GeneratorAnalysis" value="1" />
    <!  secondary mass constraint stuff  >
    <parameter name="nMassConstraints" value="2" />
    <parameter name="SecondaryMasses" type="FloatVec"> 0.1349766 </parameter>
    <parameter name="SecondaryNCharged" type="IntVec"> 0 </parameter>
    <parameter name="SecondaryNNeutral" type="IntVec"> 2 </parameter>
</processor>
<processor name="MyLCIOOutputProcessor" type="LCIOOutputProcessor">
    <!    standard output: full reconstruction keep all collections  >
```

```
    <parameter name="LCIOOutputFile" type="string" >
      ./myfile_OUT.slcio
    </parameter>
    <parameter name="LCIOWriteMode" type="string" value="WRITE_NEW"/>
  </processor>
</marlin>
```

Bibliography

[1] Behnke, T., Brau, J. E., Foster, B., Fuster, J., Harrison, M., Paterson, J. M., ... & Yamamoto, H. (2013). The International Linear Collider Technical Design Report-Volume 1: Executive Summary. arXiv preprint arXiv:1306.6327.

[2] Baer, H., Barklow, T., Fujii, K., Gao, Y., Hoang, A., Kanemura, S., ... & Peskin, M. E. (2013). The International Linear Collider Technical Design Report-Volume 2: physics. arXiv preprint arXiv:1306.6352.

[3] Barklow, T., Brau, J., Fujii, K., Gao, J., List, J., Walker, N., & Yokoya, K. (2015). ILC operating scenarios. arXiv preprint arXiv:1506.07830.

[4] Behnke, T. (2013). The International Linear Collider Technical Design Report-Volume 4: detectors (No. arXiv: 1306.6329; ILC-REPORT-2013-040; ANL-HEP-TR-13-20; BNL-100603-2013-IR; IRFU-13-59; CERN-ATS-2013-037; COCKCROFT-13-10; CLNS-13-2085; DESY-13-062; FERMILAB-TM-2554; IHEP-AC-ILC-2013-001; INFN-13-04-LNF; JAI-2013-001; JINR-E9-2013-35; JLAB-R-2013-01; KEK-REPORT-2013-1; KNU-CHEP-ILC-2013-1; LLNL-TR-635539; SLAC-R-1004; ILC-HIGRADE-REPORT-2013-003). Argonne National Laboratory (ANL), Argonne, IL (United States); Pacific Northwest National Laboratory (PNNL), Richland, WA (United States); SLAC National Accelerator Laboratory (SLAC), Menlo Park, CA (United States); Fermi National Accelerator Laboratory (FNAL), Batavia, IL (United States).

[5] Thomson, M. A. (2009). Particle flow calorimetry and the PandoraPFA algorithm. Nuclear Instruments and Methods in Physics Research Section A: Accelerators, Spectrometers, Detectors and Associated Equipment, 611(1), 25-40.

[6] Gaede, F., Behnke, T., Graf, N., & Johnson, T. (2003). LCIO-A persistency framework for linear collider simulation studies. arXiv preprint physics/0306114.

[7] Brun, R., & Rademakers, F. (1997). ROOT-an object oriented data analysis framework. Nuclear Instruments and Methods in Physics Research Section A: Accelerators, Spectrometers, Detectors and Associated Equipment, 389(1-2), 81-86.

[8] Olive, K. A., & Particle Data Group. (2014). Review of particle physics. Chinese physics C, 38(9), 090001.

[9] Gluckstern, R. L. (1963). Uncertainties in track momentum and direction, due to multiple scattering and measurement errors. Nuclear Instruments and Methods, 24, 381-389.

[10] Grindhammer, G., & Peters, S. (2000). The parameterized simulation of electromagnetic showers in homogeneous and sampling calorimeters. arXiv preprint hep-ex/0001020.

[11] Longo, E., & Sestili, I. (1975). Monte Carlo calculation of photon-initiated electromagnetic showers in lead glass. Nuclear Instruments and Methods, 128(2), 283-307.

[12] Wigmans, R. (2000). Calorimetry: Energy measurement in particle physics (Vol. 107). Oxford University Press.

[13] List, B., & List, J. (2009). MarlinKinfit: An object–oriented kinematic fitting package. LCTOOL-2009-001.

[14] Sjöstrand, T., Mrenna, S., & Skands, P. (2006). PYTHIA 6.4 physics and manual. Journal of High Energy Physics, 2006(05), 026.

[15] Agostinelli, S., Allison, J., Amako, K. A., Apostolakis, J., Araujo, H., Arce, P., ... & Behner, F. (2003). GEANT4—a simulation toolkit. Nuclear instruments and methods in physics research section A: Accelerators, Spectrometers, Detectors and Associated Equipment, 506(3), 250-303.